UNIVERSIDADE D
COIMBRA

Luís Henrique Coutinho Martins

Characterization of Electro-Optic Polarization Controllers for Discrete-Variable Quantum Communications Transmitters

Thesis submitted to the University of Coimbra in fulfilment of the requirements of the Master's Degree in Physics Engineering under the scientific supervision of Ph.D. Nuno João de Oliveira e Silva, Ph.D. Maria Helena Almeida Vieira Alberto and presented to the Physics Department of the Faculty of Sciences and Technology of the University of Coimbra.

October 2021

Acknowledgements

This masters dissertation would not have been possible without crucial incentives for which I will forever be grateful.

First, I would like to thank Prof. Dr. Nuno João de Oliveira e Silva for the guidance, support and knowledge shared throughout the project development. Thank you for the opportunity and belief in my capabilties.

To Prof. Dr. Maria Helena Almeida Vieira Alberto, thanks for the interest, opportunistic questions and, most importantly, the mathematical assistance. It was vital for the early progress of this work.

To Dr. Armando, Nelson, Rita, Sara and all the other members of the Group of Optical Quantum Communications and Technologies, thank you for your opinions, criticisms and readiness to help.

I also want to thank my friends for making these last few years so unique. Thank you for the patience, discussions, memories, and being by my side when I most needed it. A special acknowledgement to Afonso, Laura and Diogo for helping me grow.

Last but not least, I am grateful to my family, who are the reason I got here. To my father, my sister and especially my mother, who is my biggest supporter, thank you for your love and company each and every single day.

Resumo

A criptografia quântica é um espaço em constante desenvolvimento no qual a capacidade do hardware é um fator extremamente limitativo. Com vista a melhorar da segurança, distância e velocidade de comunicação, é necessário implementar novos componentes para aprimorar os sistemas reais e capacitá-los para replicação de sistemas teóricos. Esta dissertação foca-se na caracterização de um controlador de polarização eletro-ótico, para posterior implementação num transmissor de um sistema de distribuição de chaves quânticas com codificação na polarização de fotões únicos. Primeiramente, foi feita uma modelação matemática do componente para ser possível caracterizá-lo, atribuindo valores numéricos às variáveis do modelo. Foi ainda apresentado um método de caracterização adaptado da proposta da empresa EOSPACE, baseado em automação em Matlab e controlo remoto de controladores lógicos programáveis. O método foi empregue com o objetivo de estabelecer um padrão de valores que permitissem calibrar o dispositivo aquando o uso num sistema de transmissão. Foram obtidos valores para três testes diferentes, sendo feita uma comparação com os valores da datasheet do dispositivo e com dados teóricos. Os resultados pouco satisfatórios, suportam as críticas feitas ao método que requer hardware e software capaz de uma análise e controlo em tempo real. O longo período de tempo requerido para o processo, conjugado às condições limitativas, levam à conclusão que devem ser procurados outras técnicas com menos restrições e mais simplicidade de hardware que melhorem a qualidade dos resultados e minimizem o tempo despendido num processo de calibração.

Abstract

Quantum cryptography is a space in constant development in which hardware capacity is an extremely limiting factor. Therefore, to improve the security, distance and velocity of an established communication, it is necessary to implement new components to upgrade real systems and make them capable of replicating theoretical ones. This dissertation focuses on the characterization of an electro-optic polarization controller, which should be implemented in a transmitter of a Quantum Key Distribution system based on codification in the state of polarization of single photons. First, the device's mathematical model was made, so its characterization would be possible by attributing numerical values to the variables in the model. Furthermore, a characterization method, adapted from a proposal of EOSPACE enterprise, is presented. It is based on Matlab automation and remote control of programmable logic controllers. The employed method should establish a group of core values allowing the device to be calibrated when implemented in a transmission system. Results were obtained for three different tests and then compared to the datasheet values and theoretically gathered data. The unsatisfactory results support the criticism made to the method's hardware and software requirements, which should be capable of analyzing and controlling the system in real-time. Considering the long time required to complete this process and the associated limiting conditions, one can conclude that different techniques should be pursued. These should have fewer restrictions and more simple hardware, improving the quality of the results and minimizing the time spent in a calibration process.

Acronyms

CV-QKD - Continuous Variable - Quantum Key Distribution

CRC - Cyclical Redundancy Checking

DV-QKD - Discrete Variable - Quantum Key Distribution

EPC - Electro-Optic Polarization Controller

LP - Linear Polarizer

MUB - Mutually Unbiased Bases

PIN - Photodiode

PNS - Photon Number Splitting

PBS - Polarization Beam Splitter

PC - Polarization Controller

PDL - Polarization-Dependent Losses

PMF - Polarization-Maintaining Fiber

PMD - Polarization Mode Dispersion

PCB - Printed Circuit Board

PLC - Programmable Logic Controller

QBER - Quantum Bit Error Rate

QC - Quantum Channel

QKD - Quantum Key Distribution

QWP - Quarter-Wave Plate

RTU - Remote Terminal Unit

SPD - Single-Photon Detector

SMF - Single-Mode Fibre

SOP - State of Polarization

TM - Transverse Magnetic

TE - Transverse Electric

List of Figures

List of Tables

Contents

Chapter 1

Introduction

1.1 State of the Art

Communication between two parties relies on the security of the channel through which the information flows. Without some level of protection, an undesired third party may be eavesdropping, gaining access to the information without consent. With the expansion of the internet's tentacles into people's daily routines, the business world, and even government security, cryptography became the underlying mechanism sustaining the privacy of communications and information flow in general. Currently, we rely on classical public-key cryptography, which does not prevent eavesdroppers [2]. Classical public-key cryptography relies on number-theoretic problems, such as integer factorization, which require a massive amount of time and energy to be solved with the computation capacity available [3]. With the developments in quantum space and the upcoming quantum computers, quantum algorithms, like Grover's and Shor's algorithms, can efficiently solve these problems [4, 5].

Cryptography's role of maintaining information private allows both the transmitter and receiver at the communication endpoints to be the only intervening parties to understand the messages exchanged while possibly detecting third-party eavesdroppers [6]. Key-based cryptography is a process where the transmitter uses an encryption key to create a cryptogram. Both the key and

the message holding the information compose this cryptogram, which is sent employing a specific algorithm [4]. At the other end, the receiver uses a decryption key to gain access to the original message. Different algorithms exist and are categorized into two broad groups: symmetric algorithms, also known as one-key or secret-key algorithms, and asymmetric algorithms. In symmetric algorithms, the encryption key and the decryption key are the same, or the latter derives from the former [7]. An example of this type of encryption is the one-time pad, first proposed by Gilbert Vernam of AT&T in 1926. In this scheme, the key and the message are of the same length. The key is delivered privately ahead of time and securely stored. The transmitter adds the key and the message together, creating a cryptogram ready to be sent, and the receiver then subtracts the key from the cryptogram to access the confidential information. This key is only used once before being destroyed, removing any chance of third-party eavesdropping [6, 8]. In asymmetric algorithms, the keys used by both intervenients are different, one usually being private and the other public [4].

The main problem with key-based cryptography is, therefore, the secure distribution of a key and subsequent assurance that an eavesdropper does not obtain sufficient information about the shared key. Quantum-key distribution (QKD) allows for the exchange of cryptographic keys between both ends of a communication channel, granting information security based on the laws of Quantum Mechanics [7,9]. The only requirements are using a safe and effective protocol and having an error rate lower than a particular established threshold. A QKD protocol consists of two main steps: quantum communication succeeded by classical post-processing. First, the transmitter encodes information using prepared quantum states and sends them to a receiver through a public channel, which is open to eavesdroppers. Classical post-processing then follows. Here both intervening parties perform information reconciliation followed by privacy amplification. Applying these safety measures can increase the correlation between their key strings while reducing the eavesdropper's

knowledge to a particular established protection threshold [8, 10]. There are two general QKD schemes: continuous variable (CV)-QKD and discrete variable (DV)-QKD. In the former, field quadratures are measured with homodyne or heterodyne detection methods. In the latter, different degrees of freedom of light particles (photons) are used to encode information and are measured with the help of a single-photon detector (SPD) [7].

Several encoding methods exist, the most utilized being: phase encoding, where data is held in the phase difference between two interfering modes [7, 11, 12]; time-bin encoding, with information encoded in time slots [7, 13, 14]; and polarization encoding, where the state of polarization (SOP) of single photons carries the information [9, 12]. Polarization encoding is relevant in free-space and optical fiber communications. Even though the atmosphere does a good job maintaining the polarization of photons, polarization drift in optical fibers can be overcome [9]. In optical fiber telecommunications, the transmitting and receiving setups are adapted to both the QKD protocol adopted and the chosen encoding technique. The underlying security in these protocols relies on the no-cloning theorem and the indistinguishability of non-orthogonal quantum states. The no-cloning theorem states that no quantum state can be duplicated, no matter the computational power possessed. The fact that quantum states cannot be perfectly copied is a huge advantage comparing to classical information systems [6, 15]. Furthermore, there is no device capable of distinguishing two non-orthogonal states. With that said, a measurement cannot occur without perturbing the quantum state. In other words, measurements lead to the collapse of quantum states which is not reversible. System perturbations are detected by classical post-processing if measurements are performed by a third party, revealing eavesdropping activity.

There are several QKD protocols regarding polarization encoding. The best-known one, the BB84 protocol, was proposed by Bennett and Brassard in 1984. The logical states 0 and 1 are encoded with two non-orthogonal states each by employing two mutually unbiased bases. That is to say when a state is encoded

in one base, a measurement using the other one leads to equally probable outcomes [7, 10]. Assuming the transmitter has a single-photon source, he encodes a photon in one of four states and sends it through a quantum channel. The receiver then chooses a base and measures it. This procedure is reproduced numerous times until each has a sequence of N pairs (bit, base). Here the post-processing phase starts, where both parties communicate over a classical channel. They compare the bases used to send and measure the quantum bits, only keeping the bits where the bases match. Now they both have an N/2 bit string referred to as the *raw key*. At this point, both parties have to check if the error rate is acceptable by disclosing a sample of bits, allowing them to realize the presence of an eventual eavesdropper. At the end of this stage, an utterly secret key has been shared with success, or an eavesdropping third party was detected trying to access the shared information [10].

Many other protocols followed. In 1992, Bennett proposed the B92 protocol, a simple communication protocol showing that only two non-orthogonal states are necessary. The transmitter associates the values 0 and 1 to one of two quantum states from different bases. By detecting in one of two mutually unbiased bases, the receiver will have both conclusive and inconclusive results, leading to both parties discarding the latter as the former yield the result of the bit sent [7, 16]. This protocol is very loss-dependent since an eavesdropper can make these measurements, obtain the same results, and compensate for inconclusive results with pulses emitted afterwards. In 1999 a 6-state protocol was proposed, respecting more the symmetry of the qubit state space. Here, the probability of both parties choosing the same base is lowered to 1/3 but, as a trade-off, this protocol simplifies the security analysis as the eavesdropper's job gets much more complicated, better key generation rates are achieved, and noise tolerance is boosted [6, 17]. In 2004, the SAGR04 protocol was introduced, giving a more complex alternative to the BB84 protocol when working with attenuated lasers. It was developed to help counter photon number splitting (PNS) attacks due to the challenge of having single-photon sources in

practice [16, 18, 19]. The idea is that an eavesdropper can count the number of photons sent in a pulse, and if the number is greater than one, he can steal the excess photons, gaining information without being detected. The encoding and emission of photons are similar to the BB84 protocol but, instead of announcing the bases used, the transmitter announces a pair of non-orthogonal quantum states used to encode the qubit sent [16, 18]. Other alternatives exist for different types of communication regarding entanglement, continuous variables or even different degrees of freedom other than polarization. The objective is to make the system reliable to any attack possible, even with all the computational power available. No collective or coherent attacks should affect the performance of a point-to-point link. [2]

QKD setups have evolved to overcome several challenges. In pursuit of high-performance at low costs, software and hardware solutions are constantly being pursued [2]. Single-photon sources are essential to execute the BB84 protocol. These sources are tough to produce, so attenuated laser pulses are employed instead. These have a low probability of generating more than one photon per pulse, closing the door to PNS attacks [6, 16]. Detector technology research has been fundamental in searching for quantum efficiency and low dark counts [20, 21]. Low noise in single-photon detectors is a critical factor in enabling more distant connections [2]. In fibre-based QKD, low losses and low attenuation in the quantum channel is vital for extending the communication range and increasing the transmission bit rate. Single-mode fibre (SMF), which has a small enough core to guide only one spatial mode, is suited for quantum communications. Multi-mode fibres are not fitting, as modes can easily interfere with each other, jeopardizing the isolated systems (qubits). Several polarization effects introduce transmission losses. One can observe a geometrical phase when the propagation vector suffers an adiabatic change, causing a propagating mode to rotate. As input and output need to be aligned, active feedback mechanisms may be required. Birefringence is another effect that occurs due to orthogonal modes propagating along the fibre having different

phase velocities. It is similar to the geometrical phase but may also affect ellipticity. If thermal and mechanical conditions are stable or change slowly, it can easily be compensated for. Much research has been conducted on Polarization Mode Dispersion (PMD) as well. This effect originates in the SMF birefringence and significantly impacts long-distance communication because it grows with the fibre length [6, 22–24]. Low cost and system robustness are also indispensable research topics when striving for real-world applications. Communications at room temperature have already been demonstrated possible over a 100-kilometre distance [2], and even greater distances have been reached, but due to channel losses detectors cannot withstand, different solutions are being constantly sought. Advanced new technology, like a quantum repeater [25], has been a focal point in the field as professionals aim for more considerable distances.

From a transmission point of view, quickly changing the SOP of photons boosts the bit generation rate. Currently, classical optical communications deliver speeds of 100 Gbit/s per wavelength channel, while QKD still operates at rates of a few Mbit/s [2]. As controlling the SOP of qubits and switching between states at high speeds enables high key generation rates, having a high-speed polarization modulator is extremely important [26]. SOP generation and control hardware research is then a critical component of the future development of QKD. Complex setups using phase modulators, polarization beam splitters and polarization-maintaining fibre have been proposed [9,27,28] but due to their complexity and high costs, other solutions are currently being sought.

1.2 Motivation and Goals

The field of quantum technologies has still a lot to develop, and better hardware implementations for QKD protocols is vital for future progress. Thus, the opportunity arose to embrace a project within the Optical Quantum Commu-

nications and Technologies Group at the Instituto de Telecomunicações (IT) at the University of Aveiro. The aim is to find and analyze better hardware for the DV-QKD setup. On the transmitter side, an Electrical Polarization Controller working with mechanical components is currently set. A better alternative that can more rapidly and accurately define any desired SOP is this research's focus. An electro-optic polarization controller should increase the velocity and stability of the setup's transmitter, covering some of its limitations. In this dissertation, an electro-optic polarization controller is studied. A mathematical modelling followed by a characterization of the component is presented to assess the validity of the proposed characterization method. A better understanding of the studied component should help the final goal of substituting the hardware currently in place.

1.3 Dissertation Outline

This dissertation consists of 5 chapters. The document structure and the information yielded in each chapter is now presented:

- **Chapter 1** yields the state-of-the-art and the motivation and goals for this dissertation.
- **Chapter 2** has a brief explanation of theoretical concepts vital for understanding polarization, quantum key distribution and the propagation of light.
- **Chapter 3** describes the mathematical concepts related to light propagation through a medium, followed by the mathematical modelling of the EOSPACE electro-optic polarization controller, finishing with the characterization methodology proposed.
- **Chapter 4** incorporates the results and data analysis.
- **Chapter 5** summarizes the conclusions on the adopted methodology and gives some insight into possible further work.

Chapter 2

Theoretical Review

This chapter goes over the basic mathematical and theoretical concepts needed to understand polarization and QKD systems. The content addressed is in line with the practical work developed in the dissertation. First, an overview of two different formalisms for the mathematical characterization of polarization is delivered. Then, a theoretical introduction to the qubit and QKD implementation follows. This chapter then concludes with some information on practical effects to consider when looking at an optical fibre communication channel.

2.1 Mathematical Representation of Polarization

Light is said to have dual nature. It was initially characterized as a particle by Isaac Newton and as an electromagnetic wave by Christiaan Huygens [29, 30]. Both the discrete and continuous behaviours are vital as they complement each other in our understanding of light. Phenomena that highlight its interaction with matter, like the photoelectric effect, display its particle nature. On the other hand, its electromagnetic nature describes optical phenomena and light propagation. Maxwell was the one who successfully set forth a unified theory of electromagnetic radiation which accurately represents light mathematically. What we casually refer to as light represents not only

visible light but a vast spectrum of electromagnetic radiation with a broad range of wavelengths.

Electromagnetic radiation is a transverse wave where the electromagnetic field oscillates perpendicularly to the direction of propagation. Polarization is a fundamental property of light defined by the motion of the electric field [31]. The direction of the electric field vector $\vec{E}(x, y, z, t)$ at any given point in time and space will determine the SOP of the light wave. We can decompose an electromagnetic plane wave and then express it by two orthogonal components along the x-axis and the y-axis, describing two plane waves orthogonal to each other at a point in space

$$\vec{E} = \hat{x}E_{ox}e^{i(kz-\omega t+\delta_x)} + \hat{y}E_{oy}e^{i(kz-\omega t+\delta_y)} \tag{2.1}$$

where $kz - \omega t$ is the propagator and δ_x and δ_y are the phases of the x and y components, respectively. Every SOP can then be given, in general, by a polarization ellipse

$$\frac{E_x^2}{E_{0x}^2} + \frac{E_y^2}{E_{0y}^2} - 2\frac{E_x}{E_{0x}}\frac{E_y}{E_{0y}}\cos\delta = \sin^2\delta \tag{2.2}$$

where $\delta = \delta_x - \delta_y$ is the phase difference. For specific conditions of amplitude, phase difference and orientation, one obtains particular linear or circular polarization states [30, 32]. Two types of formalism for mathematical representation of optical waves allowing polarization analysis are now described in more detail.

2.1.1 Jones Formalism

Robert Clark Jones developed a matrix formalism used to characterize polarization through amplitude and phase. Jones formalism is very useful when treating problems in which optical beams are added to each other, and there is a phase and amplitude relation between them. This formalism comprises 2×1 column vectors, the Jones vectors, and 2×2 matrices, the Jones matrices, representing polarization states and optical components, respectively,

where complex quantities are often used. The equation 2.1 can be split into two separate components to write the Jones vector

$$\mathbf{E} = \begin{pmatrix} E_{ox}e^{i(kz-\omega t+\delta_x)} \\ E_{oy}e^{i(kz-\omega t+\delta_y)} \end{pmatrix}. \tag{2.3}$$

By suppressing the propagation factor $kz - \omega t$ we obtain the simplified Jones vector

$$\mathbf{E} = \begin{pmatrix} E_x \\ E_y \end{pmatrix} = \begin{pmatrix} E_{ox}e^{\delta_x} \\ E_{oy}e^{\delta_y} \end{pmatrix} \tag{2.4}$$

where E_x and E_y correspond to the complex amplitudes defining a general elliptical SOP [30]. As it is usually easier to work utilizing normalized Jones vectors, one can rewrite matrix 2.4 as

$$\mathbf{E} = \frac{1}{\sqrt{(E_{ox})^2 + (E_{oy})^2}} \begin{pmatrix} E_x \\ E_y \end{pmatrix} \tag{2.5}$$

where $I = (E_{ox})^2 + (E_{oy})^2 = (E_0)^2$ is the intensity of the optical field set as $(E_0)^2 = 1$ for a normalized Jones vector. Given the mathematical formulation above, depending on both the amplitudes, E_{ox} and E_{oy}, and the phase difference δ, completely polarized light is described. The SOP of interest are summarized in table 2.1.

Symbol	SOP	Jones Vector
$\|H\rangle$	Horizontal	$\mathbf{E} = \begin{pmatrix} 1 \\ 0 \end{pmatrix}$
$\|V\rangle$	Vertical	$\mathbf{E} = \begin{pmatrix} 0 \\ 1 \end{pmatrix}$
$\|D\rangle$	Diagonal (Linear $+45^{\mathrm{o}}$)	$\mathbf{E} = \frac{1}{\sqrt{2}} \begin{pmatrix} 1 \\ 1 \end{pmatrix}$
$\|A\rangle$	Anti-Diagonal (Linear -45^{o})	$\mathbf{E} = \frac{1}{\sqrt{2}} \begin{pmatrix} 1 \\ -1 \end{pmatrix}$
$\|R\rangle$	Right-hand Circular	$\mathbf{E} = \frac{1}{\sqrt{2}} \begin{pmatrix} 1 \\ i \end{pmatrix}$
$\|L\rangle$	Left-hand Circular	$\mathbf{E} = \frac{1}{\sqrt{2}} \begin{pmatrix} 1 \\ -i \end{pmatrix}$

Table 2.1: Jones Vectors for main SOP

The Jones formalism also sets the matrix form for various optical elements like polarizers, retarders and rotators. One can relate the polarization of a light wave at the input of one of these elements with the output polarization using the Jones matrices characterizing the ongoing transformation. The relation can be written as

$$\begin{pmatrix} E_x^{'} \\ E_y^{'} \end{pmatrix} = \begin{pmatrix} j_{xx} & j_{xy} \\ j_{yx} & j_{yy} \end{pmatrix} \begin{pmatrix} E_x \\ E_y \end{pmatrix} \tag{2.6}$$

where $E_x^{'}$ and $E_y^{'}$ are components of the output wave and E_x and E_y the components of the input wave. Also,

$$\mathbf{J} = \begin{pmatrix} j_{xx} & j_{xy} \\ j_{yx} & j_{yy} \end{pmatrix} \tag{2.7}$$

is the Jones matrix relating the two waves and characterizing the optical element in place.

2.1.2 Stokes Formalism

Alternatively to the Jones formalism, the Stokes formalism offers another very convenient way of describing polarization. In contrast to Jones formalism that uses complex numbers to characterize a particular SOP, the Stokes parameters are real quantities with dimensions of intensity that allow studying not only polarized light but also unpolarized light. These enable us to study light waves much more efficiently since intensity is easily measurable, and the parameters are more straightforward to obtain than the polarization ellipse. [30, 32, 33]

One can derive the Stokes parameters using equation 2.3 for a monochromatic wave conveniently set at $z = 0$ [30]. The Stokes vector describing a beam of light is written as

$$\mathbf{S} = \begin{pmatrix} S_0 \\ S_1 \\ S_2 \\ S_3 \end{pmatrix} = \begin{pmatrix} E_{0x}^2 + E_{0y}^2 \\ E_{0x}^2 - E_{0y}^2 \\ 2E_{0x}E_{0y}\cos\delta \\ 2E_{0x}E_{0y}\sin\delta \end{pmatrix} \tag{2.8}$$

with $I = S_0$ being the light intensity and S_1, S_2 and S_3 quantifying the polarization amount. S_1 yields the degree of horizontal or vertical polarization of the beam, S_2 the amount of diagonal or anti-diagonal polarization and S_3 the degree of right or left circular polarization [33].

By looking at the statement above, it is clear that unpolarized light yields $S_1 = S_2 = S_3 = 0$. Also, for any state of arbitrary state of polarized light, the Stokes parameters respect the inequality

$$S_0^2 \geq S_1^2 + S_2^2 + S_3^2 \tag{2.9}$$

which for perfectly polarized light, turns into the identity

$$S_0^2 = S_1^2 + S_2^2 + S_3^2 \tag{2.10}$$

Using the equality above, one can normalize the Stokes vectors and write them for the six principal polarization states.

The normalization of the Stokes vectors allows for a 3D representation of polarization on a sphere of radius one named the Poincaré sphere. This visual representation is an excellent aid for SOP visualization and representation in practical situations.

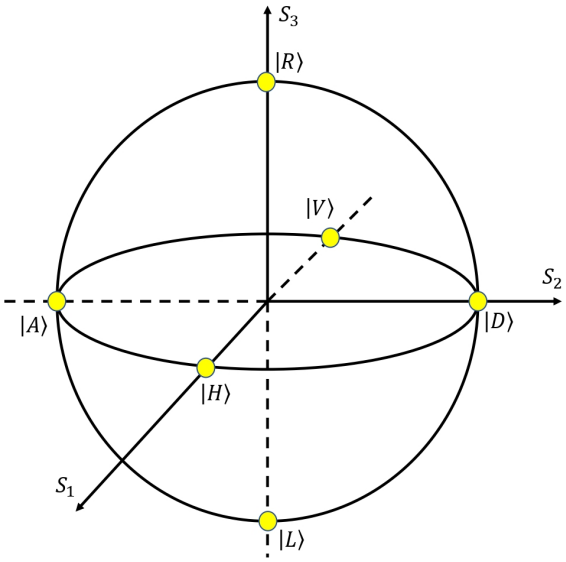

Figure 2.1: Poincaré Sphere displaying the six main polarization states

Symbol	**SOP**	**Stokes Vector**	E_{0x}	E_{0y}	δ
$\|H\rangle$	Horizontal	$\mathbf{S} = \begin{pmatrix} 1 \\ 1 \\ 0 \\ 0 \end{pmatrix}$	1	0	0^{o}
$\|V\rangle$	Vertical	$\mathbf{S} = \begin{pmatrix} 1 \\ -1 \\ 0 \\ 0 \end{pmatrix}$	0	1	0^{o}
$\|D\rangle$	Diagonal (Linear $+45^{\text{o}}$)	$\mathbf{S} = \begin{pmatrix} 1 \\ 0 \\ 1 \\ 0 \end{pmatrix}$	1	1	0^{o}
$\|A\rangle$	Anti-Diagonal (Linear -45^{o})	$\mathbf{S} = \begin{pmatrix} 1 \\ 0 \\ -1 \\ 0 \end{pmatrix}$	1	1	180^{o}
$\|R\rangle$	Right-hand Circular	$\mathbf{S} = \begin{pmatrix} 1 \\ 0 \\ 0 \\ 1 \end{pmatrix}$	1	1	90^{o}
$\|L\rangle$	Left-hand Circular	$\mathbf{S} = \begin{pmatrix} 1 \\ 0 \\ 0 \\ -1 \end{pmatrix}$	1	1	-90^{o}

Table 2.2: Stokes Vectors for main SOP

The Stokes formalism, similar to the Jones formalism, has a mathematical way of characterizing optical elements in the path of a light beam which, by interaction, can change the SOP. Given the Stokes vectors $\mathbf{S}'$ and $\mathbf{S}$ yielding

the parameters of the emerging and incident beam, respectively, one can write $\mathbf{S}^{'}$ in function of $\mathbf{S}$ as

$$\mathbf{S}^{'} = \mathbf{M} \cdot \mathbf{S} \tag{2.11}$$

or

$$\begin{pmatrix} S_0' \\ S_1' \\ S_2' \\ S_3' \end{pmatrix} = \begin{pmatrix} m_{00} & m_{01} & m_{02} & m_{03} \\ m_{10} & m_{11} & m_{12} & m_{13} \\ m_{20} & m_{21} & m_{22} & m_{23} \\ m_{30} & m_{31} & m_{32} & m_{33} \end{pmatrix} \begin{pmatrix} S_0 \\ S_1 \\ S_2 \\ S_3 \end{pmatrix} \tag{2.12}$$

where $\mathbf{M}$ is the Mueller matrix, named after Hans Mueller, characterizing the optical component [30]. If a light beam passes through n optical components, the transformation of the overall optical system is given by matrix concatenation [34].

$$\mathbf{M} = \mathbf{M}_n ... \mathbf{M}_1 \tag{2.13}$$

This relation is also true for Jones matrices since the components of the matrix 2.3 can be obtained from Stokes vectors using the following relations [30].

$$j_{xx} = \frac{S_0 + S_1}{2} \; ; \; j_{yy} = \frac{S_0 - S_1}{2} \; ; \; j_{xy} = \frac{S_2 - iS_3}{2} \; ; \; j_{yx} = \frac{S_2 + iS_3}{2} \tag{2.14}$$

2.2 Discrete Variable Quantum Key Distribution

2.2.1 Qubit

In the classical realm, the smallest unit of information is called a bit, and it can take two values, either 0 or 1. These two mutually exclusive states are easily represented by a switch that turns on and off, or by anything else that can only be in one of two states. In the quantum realm, though, this two-state

rule does not work the same way. A qubit, similar to a classical bit, can take both the values 0 or 1, but it differs from a bit because it can also take a value given by the superposition of the two individuals states [5].

A qubit is represented as a vector in a Hilbert space drawn by two basic vectors

$$|0\rangle = \begin{pmatrix} 1 \\ 0 \end{pmatrix} \; ; \; |1\rangle = \begin{pmatrix} 0 \\ 1 \end{pmatrix} . \tag{2.15}$$

A linear superposition of these two base states presents a general state for a qubit that can be written as

$$|\psi\rangle = \alpha\,|0\rangle + \beta\,|1\rangle = \cos\frac{\theta}{2}\,|0\rangle + e^{i\phi}\sin\frac{\theta}{2}\,|1\rangle \tag{2.16}$$

with $\theta \in [0, \pi]$ and $\phi \in [0, 2\pi]$. A 3D representation of these vectors, the Bloch sphere, resembles the Poincaré sphere presented in 2.1, being utilized to represent Jones vectors corresponding directly to the states given by equation 2.16. For $\theta = 0$ or $\theta = \pi$, one obtains the base states $|0\rangle$ and $|1\rangle$ illustrated at the top and bottom of the sphere, respectively. If $\theta = \frac{\pi}{2}$, then depending on the value of ϕ the states on the sphere's equator can be obtained.

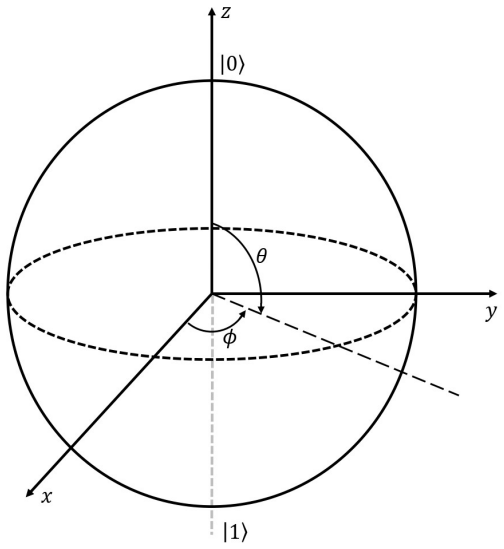

Figure 2.2: Bloch Sphere displaying the base states at the top and bottom

Physically, a qubit is a two-level quantum system. It can be the spin of an electron, the ground state and some excited state of an atom or the SOP of a light particle [35]. Photonic qubits are widely used in optical communications due to their robustness in noisy environments and fast speeds [1]. Single photons, however, are hard to realize. For this reason, faint laser pulses are a reliable photon source in QKD implementations [6].

2.2.2 DV-QKD Implementation

A DV-QKD implementation is composed of three parts: source, channel and detection. Let us focus on prepare and measure schemes based on photonic qubits. At the source, the transmitter, Alice, will prepare the qubits by encoding information in the SOP of photons. She uses at least two mutually unbiased bases (MUB) to encode information in one of two orthogonal states. In the Hilbert space defined by vectors 2.15, one can use a rectilinear base composed of horizontal and vertical polarization states, a diagonal base constituted of diagonal and anti-diagonal polarization states, and a circular base comprised of right-hand and left-hand circular polarization states. At this stage, apart from the photon source, a polarization modulator is used.

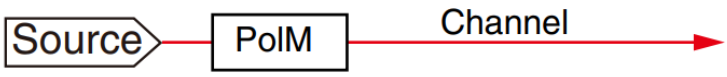

Figure 2.3: Transmitter setup with a photon source and a polarization modulator connected to the transmission channel [1]

On the detecting end, the receiver, Bob, will have to choose one MUB to measure the SOP of the arriving photon. Note that the bases utilized are decided before the communicating process but are randomly chosen when Bob is measuring. Furthermore, a measurement realized with on MUB different from the one applied by Alice when encoding the qubits will result in either

eigenstate with equal probability [16]. The base choice is made with the help of a polarization controller (PC), equivalent to a polarization modulator, and the measurement is realized by a polarization beam splitter (PBS) connected to single-photon detectors (SPD). The SPD will detect the optical signal and turn it into a measurable electric signal. An example of this setup is presented in figure 2.4.

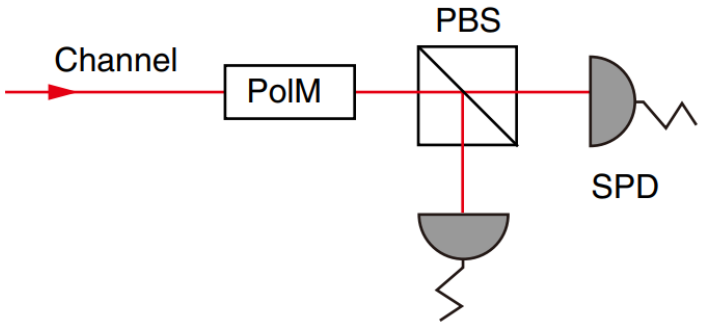

Figure 2.4: Setup at the receiving end with a PC to choose the measuring MUB and a PBS followed by two SPDs for photon detection. [1]

The channel between Alice and Bob in QKD is usually one of two channels: optical fibre or free space, the former being the choice of interest in this work. In both cases, the channel is controlled not by the communicating parties but by an eavesdropper, usually called Eve. Naturally, Eve will try to gain access to the information flow, but three quantum principles make the communication secure at the physical level [10]:

- The no-cloning theorem, which yields that no quantum state can be duplicated, preventing Eve from intercepting and copying the states sent from Alice to Bob.
- Measuring a quantum state leads to its collapse. In other words, trying to obtain information by measurement will change the original state sent by Alice, changing the qubits sent to Bob.
- Measurements are irreversible. If Eve measures a state, she cannot get the original quantum state back and resend it.

2.2.3 Cryptographic Protocol - BB84

The best-known protocol for QKD was introduced by Charles Bennett and Giles Brassard in 1984. In the BB84 protocol, Alice encodes single photons in one of four SOP using two aforementioned non-orthogonal bases. Let us suppose the linear ($\bigoplus$) and diagonal ($\bigotimes$) bases are chosen. The qubits sent will then be

- $|0_{\bigoplus}\rangle$, state $|0\rangle$ encoded using a linear base;
- $|1_{\bigoplus}\rangle$, state $|1\rangle$ encoded using a linear base;
- $|0_{\bigotimes}\rangle$, state $|0\rangle$ encoded using a diagonal base;
- $|1_{\bigotimes}\rangle$, state $|1\rangle$ encoded using a diagonal base;

The qubits are sent through a quantum channel (QC) to Bob, who chooses the base he will be using for the measurements. If he chooses correctly, the measurement yields the correct value sent by Alice. If he chooses incorrectly, the qubit will collapse in one of two states (0 or 1) with equal probability. This process is replicated N times, leaving both parties with their own list of N pairs (bit, base). Then a sifting procedure takes place where Alice and Bob communicate through a classical channel to compare the chosen MUB for each measurement, discarding the data where they have chosen differently. At this point, both should have identical keys, labelled sifted keys, of length N/2. Following this procedure, a random subset of bits is compared to compute the Quantum Bit Error Rate (QBER). If the QBER is too high, the process is nullified because Eve may be gathering information on the shared key. If the QBER is low enough to be attributed to noise or another measurement error, this subset of bits is discarded, and the remaining bits of the sifted key are kept as the first instance of the secret key. After classical post-processing and privacy amplification steps, a final secret key will be set to ensure maximum security [1, 10, 16].

2.3 SOP change in an optical system

Many errors are introduced in optical systems affecting communication stability. On the transmitter side, the difficulty of sending one photon at a time requires Alice and Bob to be aware of possible photon number splitting (PNS) attacks and possibly use some countermeasure. Moreover, dark counts happen when the detector counts a sent qubit that never really reaches the SPD on the receiving side [16].

Along the quantum channel, other problems arise, depending on the medium determined to communicate. For example, the type of fibre used is relevant when using optical fibres, and the problems associated with them have to be considered in practical implementations. In optical fibres, light is guided through the core. Depending on the diameter of a fibre's core, more or fewer modes can propagate. As modes can easily couple and interfere with qubits, single-mode fibre, which has a core small enough to guide only one mode, is best suited for quanta propagation [6]. Even so, intrinsic and extrinsic factors may alter the light's SOP, independent of the optical scheme being quantum or classical.

One effect that may arise is a geometrical phase which happens when the polarization at the output of the fibre differs from an input linear SOP by an angle. This is not a massive problem as Alice and Bob can align their systems defining correspondent linear polarization states at the start. However, if the geometrical phase changes along the channel, tracking and compensation should be done via the adoption of an active feedback mechanism. The more stable the optical fibre, the less geometrical phase is added [6].

Another significant effect is birefringence. It is defined as two orthogonal polarization modes with different phase velocities by being subjected to different refractive indexes, creating a fast and slow mode. Asymmetries cause birefringence in the fibre due to intrinsic factors or exterior stress applied to

the fibre's core [6, 36]. Consequently, it is crucial to maintain the thermal and mechanical environment stable to introduce the least amount of birefringence possible in the channel. Furthermore, birefringence will affect the linearity and ellipticity of the SOP of propagating light, so it is vital to maintain it stable so it can be compensated. A particular type of optical fibres, named polarization-maintaining fibres (PMF), are made birefringent on purpose. These are valuable when uncoupling two propagating orthogonal polarization modes and maintaining them stable along the channel. Note that all other modes evolve very quickly, making these fibres suitable only for particular regions of the QC.

One should also be aware of polarization mode dispersion (PMD), which arises from two effects in series. First, low birefringence produces two group velocities, but because this birefringence is small, the two modes can easily couple due to minor fibre imperfections. These two effects will create a phase delay altering the total phase delay as the wave propagates along the channel. The longer the channel is, the more PMD can occur, totally changing the signal being emitted. A possible solution is to increase the coupling artificially so the propagating modes do not decouple easily, resulting in a more stable signal for long-distance communication processes [6].

One final significant effect, not so much in fibres but in polarization controllers' optical waveguides, is polarization-dependent losses (PDL). It is a difference in attenuation between orthogonal polarization modes. It is usually kept stable, but random outcomes may occur when a waveguide is connected to a birefringent fibre.

Chapter 3

Project Structure and Device Analysis

This chapter describes the characterization methods used in the laboratory and the devices used in the laboratorial setup. First, there is a brief overview of the project and of its relevance. Secondly, the mathematical description of the EOSPACE Electro-optic Polarization Controller is provided. Next, the characterization method adopted, the mathematics behind it and how to execute it in the laboratory are explained in detail. A summary of the materials in the setup is also presented. Finally, the automation of the characterization process is explained.

3.1 Project Description

The transmitter of the DV-QKD setup in the laboratory has an Electronic Polarization Controller, which modulates polarization based on a fibre squeezing mechanism, including piezoelectric materials. Due to its mechanical nature, the current implementation uncalibrates quite easily and limits the state generation velocity to a few kHz. To have a more stable transmitter capable of generating polarization states at a faster rate, an implementation using an Electro-optic Polarization Controller (EPC) is being pursued. Based on the

electro-optic effect, this type of device is expected to boost the transmitter capabilities significantly.

The EOSPACE Lithium Niobate ($LiNbO_3$) Polarization Controller was the device chosen to improve the transmitter and accomplish the objectives stated above. First, a mathematical model of the EPC was developed. Secondly, a characterization method to be employed in the laboratory was proposed. The device characterization method then required software capable of automatically controlling programmable power supplies. The project culminated with the device characterization method being employed in the laboratory.

3.2 Electro-Optic Polarization Controller

3.2.1 Polarization of a Wave Propagating in a Birefringent Medium

To understand what an EPC is and how it operates, is essential to know how light propagates in birefringent mediums. As stated before, the electric field's intensity, phase and direction of propagation will define the polarization of a light particle or beam. For a wave propagating in a medium, in the z-direction, its polarization is depicted in the transverse xy-plane. One can decompose it in two orthogonal components along the x-axis and the y-axis, describing two plane waves orthogonal to each other at a point in space.

$$\vec{E} = \hat{x}E_{ox}e^{i(kz-\omega t)} + \hat{y}E_{oy}e^{i(kz-\omega t)} \tag{3.1}$$

Since the wave we describe is propagating in a birefringent medium, the phase associated with each component depends on separate refractive indexes since there will be a slow and a fast axis. As a result, we will have a fast and a slow refractive index, being $n_s > n_f$. Both components can be written as

$$E_x = E_{ox}e^{i(k_o n_f z - \omega t)} = E_{ox}e^{ik_o n_f z}e^{-i\omega t} \tag{3.2}$$

$$E_y = E_{oy}e^{i(k_o n_s z - \omega t)} = E_{oy}e^{ik_o n_s z}e^{-i\omega t} \tag{3.3}$$

where $e^{ik_o nz}$ represents the accumulated phase while propagating along the waveguide. If we consider a waveguide of length L, the matrix giving the phase retardation at the waveguide's output is

$$\begin{pmatrix} e^{ik_o n_f L} & 0 \\ 0 & e^{ik_o n_s L} \end{pmatrix} = e^{ik_o n_f L}\begin{pmatrix} 1 & 0 \\ 0 & e^{ik_o \Delta n L} \end{pmatrix} \tag{3.4}$$

where $\Delta n = n_s - n_f$, and $\tau = k_o \Delta n L$ is the phase retardation at the end of the waveguide. The global phase $e^{ik_o n_f L}$, has no physical meaning because we can always time match both components at the input of the waveguide. With that said, the retardation matrix is simply

$$\begin{pmatrix} 1 & 0 \\ 0 & e^{i\tau} \end{pmatrix} \quad . \tag{3.5}$$

3.2.2 EPC Mathematical Description

When unpolarized light is incident in a crystal, two refracted beams can be observed. Taking into account Snell's law of refraction

$$\frac{\sin\theta}{\sin\theta'} = n \tag{3.6}$$

with θ and θ' the incidence and refraction angles, respectively, and n the refractive index, the relation will hold for one beam but not for the other. We label the beam for which this law holds ordinary ray, and we call the other the extraordinary ray. Crystals where this happen are anisotropic, which means physical properties vary with direction. For example, $LiNbO_3$ is an anisotropic uniaxial crystal. It has an optic axis (indicating a direction and not a single line) working as a reference for its anisotropy. In uniaxial crystals, if light travels along the optic axis, there is no birefringence to be seen. However, if

incident light makes a 90^{o} angle to the axis, ordinary rays and extraordinary rays propagate with different velocities [36].

The EOSPACE EPC is composed of a $LiNbO_3$ crystal substrate. $LiNbO_3$, a negative uniaxial crystal, has two different refractive indexes, an ordinary one and an extraordinary one, the former being bigger than the latter. This EPC can be used as a fast polarization modulator because the substrate birefringence varies linearly with an applied external electric field. This characteristic found in several uniaxial crystals is known as Pockels' electro-optic effect [36]. The external electric field is generated by applying voltages to electrodes present on the EPC's structure. The EPC comprises several stages in series, which can be mathematically modelled to thoroughly understand the polarization transformation occurring along the EPC's waveguide.

Figure 3.1: Image of the actual EOSPACE Polarization Controller with the pins to apply voltages on the bottom. Each sequence of 3 pins is linked to one stage

Each stage of the EPC acts as a linear wave plate at an angle. These can apply a phase retardation between orthogonal polarization components while having the fast and slow axes at an angle ϕ regarding the crystal's principal x and y axes. Below one can see one stage's structure: a $LiNbO_3$ birefringent substrate, a centralized waveguide for wave propagation which supports one Transverse Electric (TE) and one Transverse Magnetic (TM) modes and three parallel electrodes, a central one on top of the waveguide, which is grounded, and the other two on the sides where the polarization controlling voltages are applied [37].

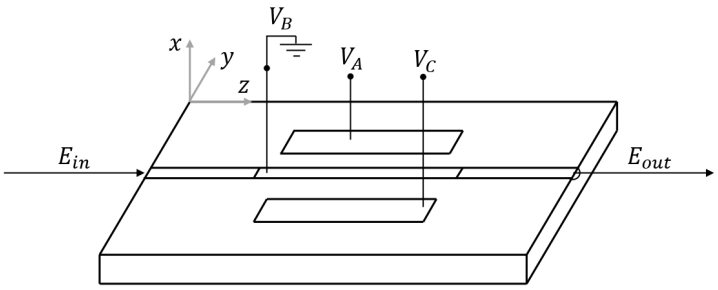

Figure 3.2: Model of one stage of the EPC showing the electrodes and waveguide in the z-direction on top of a $LiNbO_3$ substrate.

To mathematically describe the physical transformation occurring along the EPC's waveguide, we use equation 2.5 to describe our polarization at the waveguide's input. The transformation matrix M, characterizing the propagation along the waveguide, has three components regarding three operations we have to take into account:

1. Firstly, we apply a rotation matrix R to do calculations in the coordinate system $x^{'}y^{'}$ at an angle ϕ relative to the original xy coordinate system

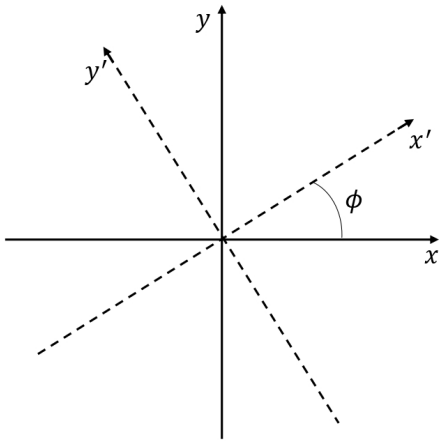

Figure 3.3: Change of coordinate system made when calculating the phase difference between orthogonal components

where the matrix describing the rotation is

$$R(-\phi) = \begin{pmatrix} \cos\phi & -\sin\phi \\ \sin\phi & \cos\phi \end{pmatrix} \tag{3.7}$$

2. Now that we are acting over the coordinate system aligned with the fast and slow axes, the phase retardation matrix $T(\tau)$, given by equation 3.5, is applied.

3. At last, a reverse rotation matrix is multiplied so the polarization at the output of the waveguide, E_{out}, is expressed in the original xy coordinate system.

$$R(\phi) = \begin{pmatrix} \cos\phi & \sin\phi \\ -\sin\phi & \cos\phi \end{pmatrix} \tag{3.8}$$

In the end, for an arbitrary input, our output can be written as

$$E_{out} = R(\phi)T(\tau)R(-\phi)E_{in} \Rightarrow E_{out} = ME_{in} \tag{3.9}$$

where M is the matrix that characterizes the polarization conversion, while E_{out} is the normalized Jones vector representing the output polarization. After some calculations, we have

$$E_{out} = \begin{pmatrix} \cos^2\phi + e^{i\tau}\sin^2\phi & \sin\phi\,\cos\phi\,(e^{i\tau}-1) \\ \sin\phi\,\cos\phi\,(e^{i\tau}-1) & \sin^2\phi + e^{i\tau}\cos^2\phi \end{pmatrix} E_{in}\ . \tag{3.10}$$

This SOP transformation can also be written using Stokes notation by employing a Mueller matrix for a rotated waveplate.

$$\vec{S}_{out} = \begin{pmatrix} \cos^2(2\phi) + \sin^2(2\phi)\cos(\tau) & \frac{1}{2}(\cos(\tau)-1)\sin(4\phi) & \sin(\tau)\sin(2\phi) \\ \frac{1}{2}(\cos(\tau)-1)\sin(4\phi) & \sin^2(2\phi) + \cos^2(2\phi)\cos(\tau) & -\sin(\tau)\cos(2\phi) \\ -\sin(\tau)\sin(2\phi) & \sin(\tau)\cos(2\phi) & \cos(\tau) \end{pmatrix} \vec{S}_{in}\ . \tag{3.11}$$

The SOP change can be graphically observed as a Stokes parameter representation in the Poincaré Sphere. The angle ϕ defines a rotation axis starting at

S_1 along the equator, and the phase shift is simply a rotation about this same rotation axis.

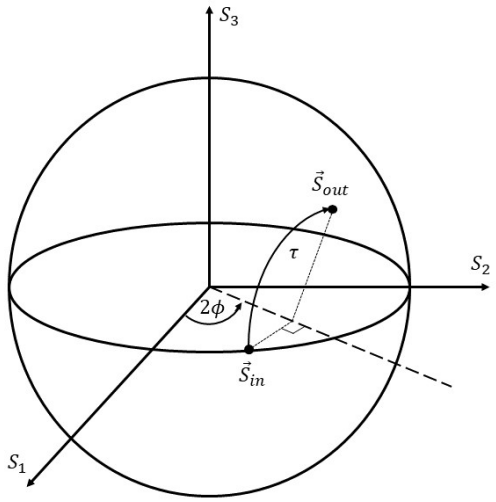

Figure 3.4: Change of SOP in the Poincaré Sphere

The angle ϕ and the total phase retardation τ are functions of the applied voltages [26, 37]. They can be written as

$$\phi = \frac{1}{2} \arctan \frac{\tau_1}{\tau_2} \tag{3.12}$$

$$\tau = \tau_2 \cos 2\phi - \tau_1 \sin 2\phi \tag{3.13}$$

and using some trigonometric simplifications one can obtain

$$\tau = \sqrt{\tau_1^2 + \tau_2^2} \tag{3.14}$$

where τ_1 is the retardation due to mode-coupling induced electro-optically and τ_2 is the phase retardation induced electro-optically. These two last variables vary linearly with the applied voltages but have to be corrected by a constant factor τ_i, the intrinsic phase retardation due to the birefringence of the $LiNbO_3$ crystal. This relation is given by

$$\begin{pmatrix} \tau_1 \\ \tau_2 \end{pmatrix} = \begin{pmatrix} t_{11} & t_{12} \\ t_{21} & t_{22} \end{pmatrix} \begin{pmatrix} U_s \\ U_{as} \end{pmatrix} + \begin{pmatrix} t_{1i} \\ t_{2i} \end{pmatrix} \tag{3.15}$$

where the intrinsic birefringence can be decomposed as $\tau_i^t = \begin{pmatrix} t_{1i} & t_{2i} \end{pmatrix}$, and the symmetric and asymmetric voltages are defined as $U_s = \frac{V_A+V_C}{2}$ and $U_{as} = V_A - V_C$ while the middle electrode is grounded ($V_B = 0$). Below are the mathematical expressions describing the applied voltages.

$$V_A = V_0 \frac{\tau}{\pi} \sin(2\phi) - V_\pi \frac{\tau}{2\pi} \cos(2\phi) + V_{A,Bias} \tag{3.16}$$

$$V_C = V_0 \frac{\tau}{\pi} \sin(2\phi) + V_\pi \frac{\tau}{2\pi} \cos(2\phi) + V_{C,Bias} \tag{3.17}$$

In the previous expressions, $V_{A,Bias}$ and $V_{C,Bias}$ are denominated bias voltages, and as a pair form the Bias Point. These outline the voltages required to be applied on each electrode to achieve zero birefringence for a single stage. V_0 is the needed voltage to rotate all power from the TE to the TM mode, for each stage. V_π is the voltage required to induce a 180^{o} phase shift between the TE and TM modes, for each stage. In practice, as the bias voltages already account for the intrinsic birefringence of the crystal, the parameters t_{1i} and t_{2i} can be neglected and set to zero. That change enables us to write the matrix relation in 3.15 simply as

$$\begin{pmatrix} \tau_1 \\ \tau_2 \end{pmatrix} = \begin{pmatrix} t_{11} & t_{12} \\ t_{21} & t_{22} \end{pmatrix} \begin{pmatrix} U_s \\ U_{as} \end{pmatrix} \quad . \tag{3.18}$$

Going back to 3.15, we can use the given matrix relation to write the following system of linear equations:

$$\begin{cases} \tau_1 = t_{11}U_s + t_{12}U_{as} + t_{1i} \\ \tau_2 = t_{21}U_s + t_{22}U_{as} + t_{2i} \end{cases} \tag{3.19}$$

These expressions allow the variables ϕ and τ to be written as functions of the applied voltages, providing insight into the output SOP and allowing for calculation of the system constant parameters as explained below.

The EPC can be operated in two configurations. Let us first look at the asymmetric configuration, where $U_s = 0$, by setting $V_A = -V_C$, so the voltages applied create an electric field almost only along y-direction. This operation mode exclusively induces a phase shift between the two orthogonal modes that propagate in the waveguide (EPC operated as a pure phase-shifter). Using the equation system in 3.19 one can write

$$\tau_1 = t_{12}U_{as} + t_{1i} \ , \tag{3.20}$$

$$\tau_2 = t_{22}U_{as} + t_{2i} \ . \tag{3.21}$$

As asserted earlier, in practice, the intrinsic birefringence terms t_{1i} and t_{2i} are neglected, leading to a value for τ of

$$\tau = U_{as}\sqrt{t_{12}^2 + t_{22}^2} \tag{3.22}$$

which, when equal to π, provides

$$\frac{\pi}{\sqrt{t_{12}^2 + t_{22}^2}} = U_{as} = V_\pi \ . \tag{3.23}$$

As t_{12} is usually two or more orders of magnitude smaller than t_{22}, it is a reasonable approximation to write

$$V_\pi \simeq \frac{\pi}{t_{22}} \ . \tag{3.24}$$

A similar result is realized if we set $V_A = V_C$. Here we have the symmetric configuration, where $U_{as} = 0$, and the external electric field is along the x-direction. The device operation will be focused on mode conversion (EPC operated as a pure mode-converter), and one can obtain the value for V_0

$$\tau = U_s\sqrt{t_{11}^2 + t_{21}^2} \ , \tag{3.25}$$

$$\frac{\pi}{\sqrt{t_{11}^2 + t_{21}^2}} = U_s = V_0 \ , \tag{3.26}$$

$$V_0 \simeq \frac{\pi}{t_{11}} \ . \tag{3.27}$$

These constant parameters are different for each stage and enable the device characterization, vital for calibration procedures before laboratory use.

3.2.3 Device Characterization Method

The EPC has a group of ten parameters that allow its characterization. This group comprises the constants t_{11}, t_{12}, t_{21}, t_{22}, t_{1i} and t_{2i}, which hold information about the physical properties of the EPC and will further be used to calculate the voltages $V_{A,Bias}$, $V_{C,Bias}$, V_0 and V_π. The opposite calculation can also be performed. These voltages can be visually obtained to calculate the other six parameters posteriorly. Knowing all these values, one can understand how varying the input voltages affects the input SOP and, consequently, know what voltages to apply to achieve any desired output polarization.

To determine the referred parameters, we will try to study the EPC by isolating the total retardation dependence on the applied voltages, independently of what rotation axis we set. With that in mind, Stokes notation is employed as it offers a more straightforward graphical representation of the polarization transformation using the Poincare Sphere presented in figure 3.4, and because the proposed method is based on light intensity measurements. In a birefringent medium, the transformation of an arbitrary input SOP into some output SOP is provided by 3.11. As 3.11 is really complex and our only interest is the dependence of τ on the applied voltages, we shall adjust the input and output SOP to be circularly polarized light, $\vec{S}_{in}^{t} = \vec{S}_{out}^{t} = \begin{pmatrix} 0 & 0 & \pm 1 \end{pmatrix}$. This choice of SOP grants the isolation intended, allowing us to work with a simplified form of the matrix. Moreover, the EPC can now be studied both as a pure phase shifter (asymmetric configuration) and as a pure mode converter (symmetric configuration), which would not be possible using any SOP on the S_1S_2 plane at the input since some pairs of input voltages do not allow for an output to be

obtained. Such cases happen when the rotation axis coincides with the input SOP's direction, not allowing for a rotation over it, meaning no phase shift rotation occurs. This situation can be easily visualized in figure 3.4.

To start the characterization procedure, one must set a circular polarization at the input through a linear polarizer (LP) and a polarization controller (PC) with SMF accounting for a quarter-wave plate (QWP). After propagation through the EPC, the SOP at its output will be

$$\vec{S}_{out} = \begin{pmatrix} \sin(\tau)\sin(2\phi) \\ -\sin(\tau)\cos(2\phi) \\ \cos(\tau) \end{pmatrix} . \tag{3.28}$$

The dependence on the total retardation is still unclear as the output is not simple enough to assess it. We need to detect the output SOP, know how it changed with the applied voltages, and how that transformation reflects the total retardation. That can be accomplished by retaining the third component of the output SOP. We use another polarization controller, and attached SMF, acting like a QWP and a linear polarizer before detecting the output signal intensity with a photodiode (PIN). Then we know when there is circularly polarized light at the output of the EPC. The detected SOP will be

$$\vec{S}_{detected} = \begin{pmatrix} 0 \\ 0 \\ \cos(\tau) \end{pmatrix} . \tag{3.29}$$

The previous vector shows a detected signal varying periodically with τ. The signal has maximum intensity when $\tau = 2k\pi$ rad, with $k = 0, 1, 2, ...$ and minimum intensity when $\tau = n\pi$ rad with $n = 1, 2, 3, ...$, both being limited by the [-80,80]V range. As the total phase shift is induced both in the x- and y-directions, the problem is two-dimensional. Combining 3.12, 3.13, 3.15 and the definitions for the symmetric and asymmetric voltages, one has the

dependence of the total phase shift on the applied voltages and the device parameters t_{11}, t_{12}, t_{21}, t_{22}, t_{1i} and t_{2i}.

$$\begin{pmatrix} -\tau\sin(2\phi) \\ \tau\cos(2\phi) \end{pmatrix} = \begin{pmatrix} t_{11} & t_{12} \\ t_{21} & t_{22} \end{pmatrix} \begin{pmatrix} \frac{1}{2} & \frac{1}{2} \\ -1 & 1 \end{pmatrix} \begin{pmatrix} V_C \\ V_A \end{pmatrix} + \begin{pmatrix} t_{1i} \\ t_{2i} \end{pmatrix} \tag{3.30}$$

The objective is to obtain the EPC's intrinsic parameters, so we have to sweep both V_A and V_C and plot the $\cos(\tau)$ dependence of the PIN intensity on a 2D pattern where both the maximum and minimum signal intensities are easily recognized. This pattern will be obtained using MatLab programming environment, where the sweeping process is also automated.

Two programmable power supplies, with a 200V output each, are used on the stage under test to sweep the voltages and obtain fair results. So a polarization drift along the waveguide does not occur, all remaining stages require their electrodes to have the respective bias voltages applied. This is accomplished through a Printed Circuit Board (PCB), connecting each electrode to a 30V power supply. This PCB board has one manually controllable potentiometer for every electrode not grounded, allowing for the bias voltages to be set with precision. A laboratorial setup scheme proposition is presented below.

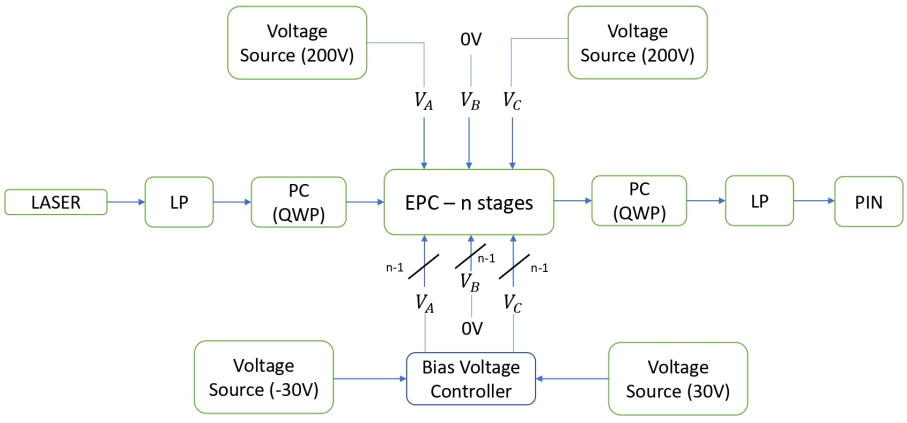

Figure 3.5: Laboratorial scheme proposition for characterization of the EPC

Notice that if the laser is already linearly polarized, the first LP is redundant and can be taken off. The LP at the output can also be replaced by a polariza-

tion beam splitter (PBS), which performs the desired output signal analysis. With those adjustments, the actual laboratorial setup is presented below.

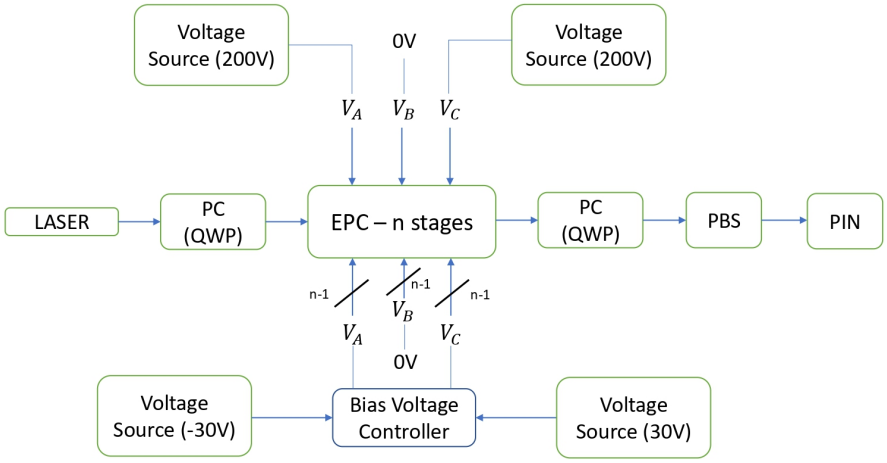

Figure 3.6: Actual laboratorial scheme used for characterization of the EPC

Fitting the mathematical description above to the data obtained with the software, one can retrieve the intrinsic device parameters and then utilize them to derive the voltages V_0 and V_π, as well as the bias voltages $V_{A,Bias}$ and $V_{C,Bias}$. These voltages can also be estimated from the 2D pattern and then used to calculate the intrinsic parameters.

Lets initially look at the first approach. When $\tau = \pi$, varying ϕ from 0 to π, traces an ellipse corresponding to the first null of the 2D pattern. In this region, the voltage pairs (V_A,V_C) allow the calculation of the intrinsic parameters. Such can be accomplished using the following mathematical relation between the parameters, the voltages and the retardations:

$$\begin{pmatrix} V_C \\ V_A \end{pmatrix} = \begin{pmatrix} \frac{1}{2} & \frac{1}{2} \\ -1 & 1 \end{pmatrix}^{-1} \begin{pmatrix} t_{11} & t_{12} \\ t_{21} & t_{22} \end{pmatrix}^{-1} \begin{pmatrix} \tau_1 - t_{1i} \\ \tau_2 - t_{2i} \end{pmatrix} \tag{3.31}$$

which translates into two equations for each voltage pair. Using the approximation $t_{12} = 0$ one can write:

$$V_C = \frac{(\tau_1 - t_{1i})(t_{22} + \frac{t_{21}}{2}) - (\tau_2 - t_{2i})\frac{t_{11}}{2}}{t_{11}t_{22}} \ , \tag{3.32}$$

$$V_A = \frac{(\tau_1 - t_{1i})(t_{22} - \frac{t_{21}}{2}) + (\tau_2 - t_{2i})\frac{t_{11}}{2}}{t_{11}t_{22}} \ . \tag{3.33}$$

As for the first null $\tau_1 = -\pi\sin(2\phi)$ and $\tau_2 = \pi\cos(2\phi)$, adding the fact that for each pair of voltages a new variable is introduced, that is, a different value of ϕ, the mathematical formalism is fit to the 2D pattern. Rearranging 3.32 and 3.33, for each pair of voltages j one obtains

$$V_{Cj} = \frac{-(\pi\sin(2\phi_j) + t_{1i})(t_{22} + \frac{t_{21}}{2}) - (\pi\cos(2\phi_j) - t_{2i})\frac{t_{11}}{2}}{t_{11}t_{22}} \ , \tag{3.34}$$

$$V_{Aj} = \frac{-(\pi\sin(2\phi_j) + t_{1i})(t_{22} - \frac{t_{21}}{2}) + (\pi\cos(2\phi_j) - t_{2i})\frac{t_{11}}{2}}{t_{11}t_{22}} \ . \tag{3.35}$$

Using the calculated parameters it is then possible to start obtaining the voltage requirements to operate the EPC. Starting with the bias voltages, given by a similar relation to 3.31, when $\tau_1 = \tau_2 = 0$:

$$\begin{pmatrix} V_{C,Bias} \\ V_{A,Bias} \end{pmatrix} = -\begin{pmatrix} \frac{1}{2} & \frac{1}{2} \\ -1 & 1 \end{pmatrix}^{-1} \begin{pmatrix} t_{11} & t_{12} \\ t_{21} & t_{22} \end{pmatrix}^{-1} \begin{pmatrix} t_{1i} \\ t_{2i} \end{pmatrix} \ . \tag{3.36}$$

At last, the mathematical description regarding the asymmetric regime, from 3.22 through 3.24, is used to obtain the value for V_π. To obtain V_0 is employed the mathematical descripton of the symmetric regime, from 3.25 through 3.27.

The second approach is based on the visualization of the 2D pattern. First, we estimate the Bias Point from the centre of the elliptical pattern. Secondly, we trace the -1 and $+1$ diagonals crossing the Bias Point. Here we notice that these two lines intersect the first null in four different points, from which four voltage pairs are acquired. These voltage pairs correspond to four positions different positions of the rotation axis on the Poincaré Sphere's equator: $\phi = 0$, $\phi = \frac{\pi}{4}$, $\phi = \frac{\pi}{2}$ and $\phi = \frac{3\pi}{4}$.

When $\phi = 0$, the EPC is being operated as a pure phase shifter, and one can estimate the voltage parameter V_π from the elliptical pattern using the Pythagorean theorem. The mathematical procedure for this calculation is

$$V_A^2 + V_C^2 = V_X^2 \tag{3.37}$$

where V_X marks the distance from the Bias Point to the intersection of the $+1$ diagonal with the first null. Knowing $V_A = -V_C$, and using the definition of asymmetric voltage combined with equation 3.23, one ends up getting

$$V_X = \frac{V_\pi}{\sqrt{2}} \ . \tag{3.38}$$

When $\phi = \frac{\pi}{4}$, the EPC works as a pure mode converter, and one can estimate the voltage parameter V_0 from the elliptical pattern using the Pythagorean theorem. The mathematical procedure is similar to the previous one. One applies equation 3.37, but this time V_X marks the distance from the Bias Point to the intersection of the -1 diagonal with the first null. Knowing $V_A = V_C$, and using the definition of symmetric voltage combined with equation 3.26, one ends up getting

$$V_X = \sqrt{2}V_0 \ . \tag{3.39}$$

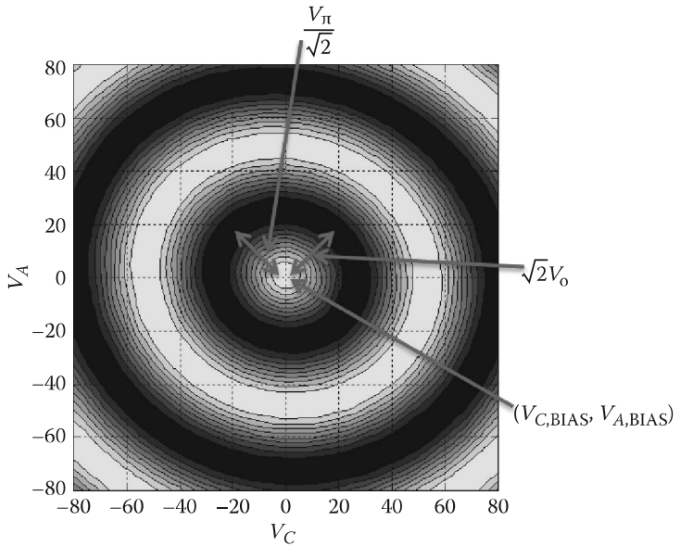

Figure 3.7: 2D elliptical pattern with visual estimation of the voltage parameters V_π, V_0, $V_{A,Bias}$ and $V_{C,Bias}$

Having calculated the voltage parameters, 3.19 and 3.36 are used to obtain the other six parameters using MatLab software. To assess the quality of the values collected, the mathematical formulation is employed to build a theoretical 2D pattern using the obtained parameters.

3.2.4 Description of Setup Components

To further understand the setup presented for the characterization process, let us describe the setup's main components:

Laser Source

The laser source is a continuous light source with a 1539.77 nm wavelength and a maximum output power of +12.5 dBm. The laser's output power was set at -3 dBm, and the light was confirmed to be horizontally polarized with the help of a polarimeter.

Polarization Controller as QWP:

QWPs are the simplest device for producing and detecting circularly polarized light [36]. Two manual PCs are operating as QWP in the setup. The first one will guarantee a circular SOP at the EPC's input while the one at the output makes the inverse transformation, enabling the detection procedure. These two QWPs allow us to analyze the progress of a linear input with the simple dependence on $\cos(\tau)$. The Jones matrix for a linear QWP with the fast axis at 0^{o} is

$$\begin{pmatrix} e^{i\frac{\pi}{4}} & 0 \\ 0 & e^{-i\frac{\pi}{4}} \end{pmatrix} . \tag{3.40}$$

Polarization Beam Splitter

On the detecting end of the setup, after the QWP, is placed a PBS, which uses birefringent materials to split the light beam into two orthogonal components. In this case, the PBS aligns at 0^{o}, so the orthogonal components are horizontal and vertical.

Photodiode (PIN) + Arduino

The PIN, a semiconductor capable of turning light intensity into a measurable current, is placed after the PBS. When the EPC input and output signals are the same, the PBS will analyze and let through light with maximum intensity. This is how we identify the Bias Point, for example. The intensity variation detected by the PIN is communicated to the software through an Arduino Due, allowing the 2D elliptical pattern to be built. It is nothing more than the plot of the intensity measured by the PIN against the varying voltages V_A and V_C. The PIN and Arduino may limit the characterization's speed due to the PIN's response capability to the light intensity changes or the Arduino's connection response. Nevertheless, we found a 100ms time gap to be enough to run the tests smoothly, while keeping the testing time reasonable.

Electro-Optic Polarization Controller

The EOSPACE EPC, being the core of the setup, is where all the voltages are applied to change the SOP. A 6-stage EPC is used, which acts like six different rotated wave-plates, each to be characterized separately.

30V Power Supply

This power supply has two different outputs, one providing positive voltages while the other offers negative voltages. The bias voltages are set using this power supply and should remain fixed through the whole characterization process.

Programmable Power Supplies

The programmable power supplies are connected to the stage being characterized. One is responsible for sweeping V_A while the other sweeps V_C. The model used was an Elektro-Automatik PS 5200-02, which has a 200V/2A maximum output. These only provide positive voltages, meaning negative voltages are supplied by changing the voltage output connections manually. The speed at which the EPC's characterization is performed depends on the response time of these power supplies, which have a USB response time of 2ms maximum, and a voltage regulation rise time, from 10 to 90%, of 30 ms maximum.

3.2.5 Power Supply Control and Process Automation

The characterization process was automated using the MatLab programming environment. The compiled software is composed of four different parts: a first one where the communication with the power supplies is made, and the functions required are defined; a second one where the functions are used to sweep voltages, read the signals and build the vectors where the acquired data is stored; a third part where the data is plotted to be posteriorly analyzed; a fourth and final part where parameter calculations are made and theoretical plots are built for data analysis.

Communication with the power supplies was accomplished through a Modbus RTU (remote terminal unit), a communication protocol designed for control and signal acquisition on Programmable Logic Controllers (PLCs). The message system distinguishes between query messages, that cause the device to send a response message back, and control messages, that only cause a 1:1 echo reply. Consequently, the former are read-only messages while the latter are write-only messages. These messages are written in hexadecimal notation and sent as byte structures with a specific order, allowing the PLC to distinguish different orders, functions, and values.

Let us look at the message structure to better understand how the communication process works:

1. The first byte indicates the address, which for Modbus RTU is always 0.

2. The second byte contains a Modbus function code determining whether it is a read or write message and whether one is trying to access one coil, one single register, or multiple registers. Coils are used for simple logic values of 0 or 1. Some examples could be turning the voltage output on and off or switching between manual and remote control. Registers are used for values, efficient when writing or reading voltage or current values, for example.

3. Here, the messages start to differ depending if one is sending or reading information from a coil, register or multiple registers. First, the target is to be defined. If writing data on, or reading it from, only one register or coil, the third and fourth bytes of the structure are enough to identify them. When writing to multiple registers, the third and fourth bytes identify the starting register. The two following bytes yield the number of registers. One other byte is used to count this number by holding that value squared. If values are being read from a coil, we need two bytes to identify it and two more to indicate it is only one coil. When reading from registers, the starting register is specified, followed by the number

of registers being read.

4. The following bytes are the ones holding the data being written. No data has to be specified when we want to read it, only where to read it from. When writing to a coil or a single register, only two bytes are used, but for multiple registers, one may need up to 246 bytes as 123 registers can be written with one single message.

5. The last two bytes hold the checksum to guarantee the message structure is correct and can be recognised by the PLC. A Modbus CRC-16 is employed with the given hardware. This checksum is a frame checking where 16 bits (2 bytes) are used. CRC stands for Cyclical Redundancy Checking and means the content of the entire message is verified. Furthermore, the byte order of the checksum is reversed after its calculation.

Byte 0	Byte 1	Bytes 2+3	Bytes 4+5	Bytes 6+7
Addr	FC	Start reg.	Data word	CRC
0x00	0x06	0...65535	Value to write	Checksum ModBus-CRC16 (1

(a)

Byte 0	Byte 1	Bytes 2+3	Bytes 4+5	Bytes 6+7
Addr	FC	Start reg.	Number	CRC
0x00	0x03	0...65535	Number of regs to read (1...125)	Checksum ModBus-CRC16 (1

(b)

Figure 3.8: Message structure used when a) writing a voltage value, for example, to a single register and b) when reading a value from a single register

The functions built using the Modbus RTU protocol allow us to turn the remote control on and off, turn the voltage outputs on and off, and set the desired voltages on the power supplies. The voltage sweeping process is made possible while also reading the power supplies' actual voltages when SOP measurements are taken.

The second part of the automation process holds the software used to perform the sweeping. The functions built come into play, and the electric signal provided by the PIN is read using the Arduino. This process starts with a connection moment where the Arduino connection is established, and the remote control and voltage outputs are turned on. Then, in steps of 1V, one of the voltages is swept (let us call it the swept voltage) from 0V to 80V while the other is maintained at the same value (let us call it the fixed voltage). When the 80V mark is reached, the fixed voltage increases by 1V and the swept voltage comes right back down to the 0V mark in 1V steps. Every step of the way, the voltages provided by the power supplies and the signal read at the Arduino are stored in three different vectors for later analysis. When this whole sweeping process is completed, the voltage outputs are turned off and manually changed before being turned back on. Four sweeps are necessary to obtain the complete 2D elliptical pattern.

The third part consists of utilizing the acquired data to build the graphical illustration of the method. Using Matlab's functions, both 2D and 3D displays of the data are produced. Also, to more accurately estimate the voltage parameters that characterize the EPC, the Bias Point is calculated by the software, and the -1 and $+1$ diagonals passing through it are traced. This process greatly simplifies the parameter estimation as the 1D plot of these diagonals presents the voltages necessary for the calculations.

The fourth and final part employs the data retrieved from the graphical representations obtained in the previous step and calculates the intrinsic parameters characterizing the EPC. Moreover, theoretical 2D patterns are built with the calculated parameters to assess the validity of the retrieved data.

Chapter 4

EPC Characterization

In this chapter, the results obtained in the characterization process are presented. For the data acquired to be reasonably comparable throughout the laboratory work, the laser output was maintained at -3.0dBm, while the room temperature was held at 25.0^{o}C. Also, the quarter waveplates were calibrated at the beginning of every day in which measurements were attained. The first data exhibited contains the results of the tests in which the datasheet bias voltages were applied to the stages not being examined. Then, the second set of data is presented. The bias voltages on the datasheet are used on the stages following the stage under test, while those already tested have the acquired bias voltages applied. Finally, in the last run of tests, the bias voltages obtained in the second run are applied to the stages following the stage under test. In this third acquisition, the stages already tested have the newly acquired bias voltages applied, similar to the second run.

4.1 Characterization using datasheet values

The first run of tests was performed using the datasheet bias voltages throughout the entire process. Having these values been obtained using a similar procedure to the one employed in the laboratory, and considering the $LiNbO_3$ crystal stable in different temperature conditions, one would expect similar re-

sults for the intrinsic parameters characterizing the EPC. The datasheet values for the bias voltages are presented in table 4.1.

	Stage 1	**Stage 2**	**Stage 3**	**Stage 4**	**Stage 5**	**Stage 6**
$V_{A,Bias}$ (V)	-10.7	-9.3	-8.5	-10.9	-7.4	-7.6
$V_{C,Bias}$ (V)	8.4	9.6	9.4	11.1	11.6	10.9

Table 4.1: Datasheet Bias Voltages

The graphical data acquired for each stage is displayed with some calculations of the diagonals's half periods as these will help on the parameter's calculations.

4.1.1 First Run - Stage 1

For the first stage characterization, stages 2-6 had the datasheet bias voltages applied to account for the intrinsic birefringence. The circular pattern was obtained by sweeping V_A and V_C within a [-80, 80]V range. The results obtained are graphically displayed in figure 4.1.

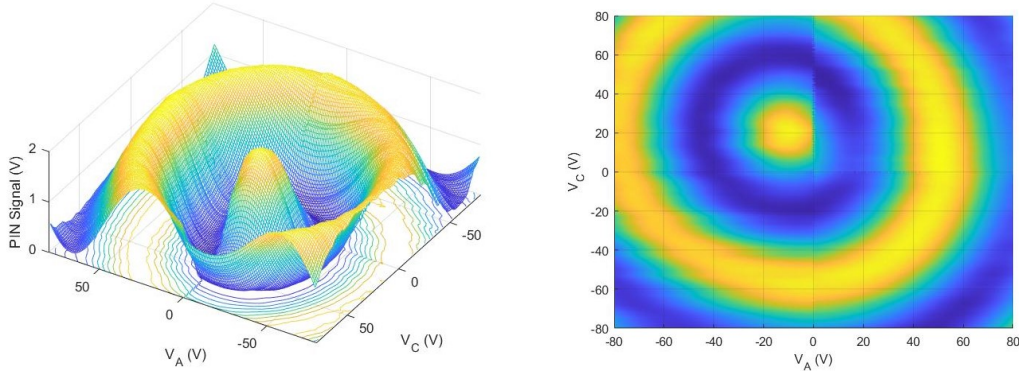

(a) (b)

Figure 4.1: Stage 1 PIN signal intensity when sweeping voltages V_A and V_C plotted a) in 3D with the contour plot underneath and b) as a 2D pattern

The Bias Point and the first null are well defined, and the pattern seems periodic, as expected. The -1 and $+1$ diagonals passing through the Bias Point,

which are used to calculate the voltage parameters V_0 and V_π, are presented below.

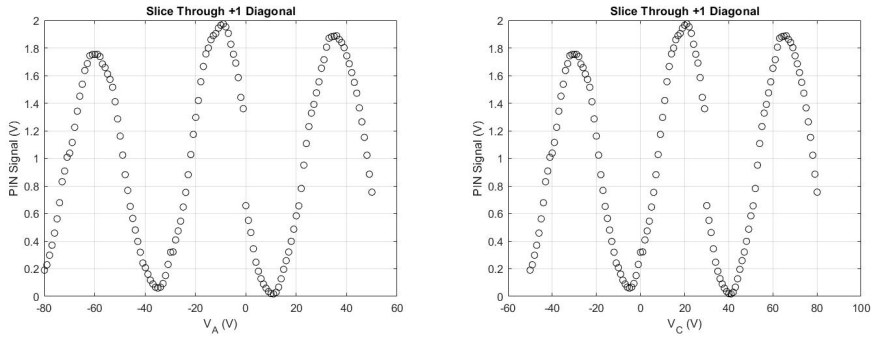

(a)

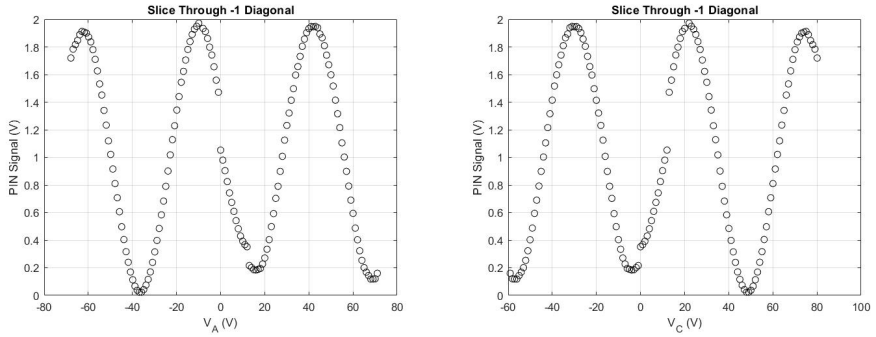

(b)

Figure 4.2: Stage 1 1D representation of the PIN signal plotted against each voltage individually where we have a) the +1 diagonal passing through the Bias Point and b) the −1 diagonal passing through the Bias Point

One would expect the peaks and valleys to have the same intensity value in a perfect periodic pattern, but a slight difference in the PIN intensity exists. There is an average half period of (24.83 ± 1.55)V along the +1 diagonal. An important detail is a gap in the data which brings the two parts of the wave closer. This gap is due to the data being acquired in quadrants because of power supply limitations. Looking at figure 4.1, the data in the top left quadrant was obtained last, and the data in the top right was obtained first. Adding to a possible delay in PIN measurements, the time separating these measurements is enough to shift the curve roughly 5V. This type of hiatus will be recurrent over measurement procedures. In the −1 diagonal, an average half

period of (26.25 ± 1.55)V is observed with no shift identifiable, even though some data gaps occur.

4.1.2 First Run - Stage 2

For the second stage characterization, stages 1 and 3-6 had the datasheet bias voltages applied to account for the intrinsic birefringence. The circular pattern was obtained by sweeping V_A and V_C within a [-80, 80]V range. The results obtained are graphically displayed in figure 4.3.

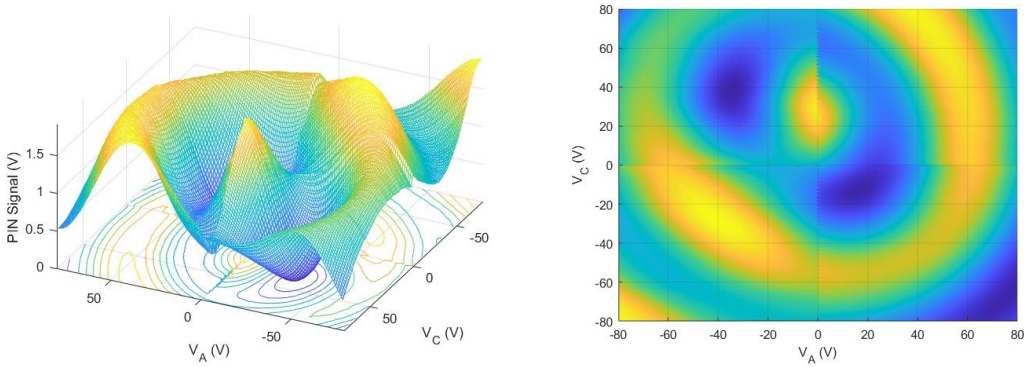

(a) (b)

Figure 4.3: Stage 2 PIN signal intensity when sweeping voltages V_A and V_C plotted a) in 3D with the contour plot underneath and b) as a 2D pattern

The Bias Point can be identified, but the first null does not show the same PIN signal intensity all around. The pattern starts looking less periodic, but its ellipticity is still identifiable. The -1 and $+1$ diagonals passing through the Bias Point, which are used to calculate the voltage parameters V_0 and V_π, are presented below.

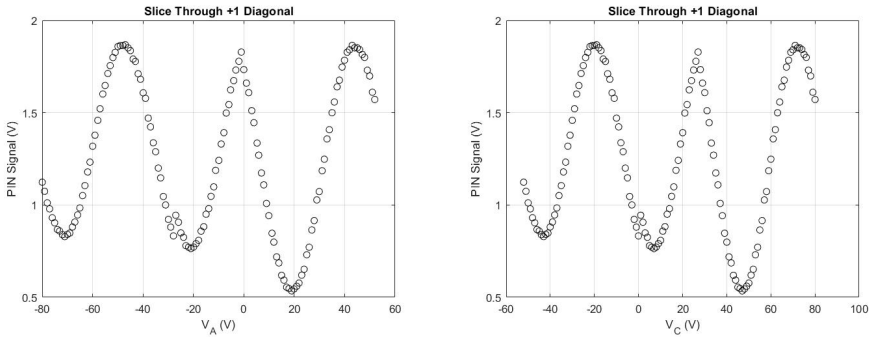

(a)

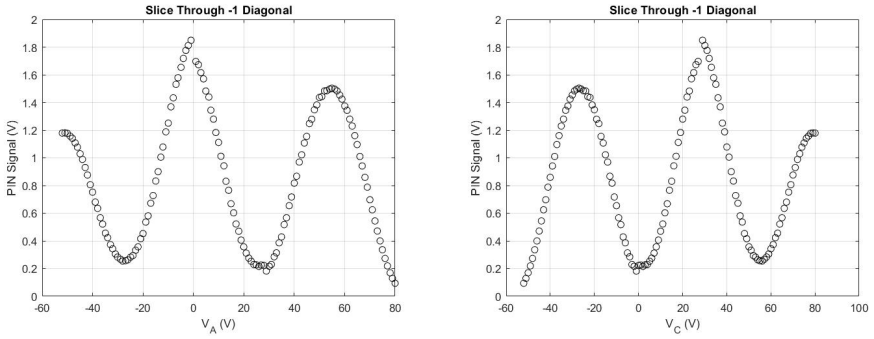

(b)

Figure 4.4: Stage 2 1D representation of the PIN signal plotted against each voltage individually where we have a) the +1 diagonal passing through the Bias Point and b) the −1 diagonal passing through the Bias Point

As expected from the 2D pattern, the peaks and valleys do not have the same intensity value as in a perfect periodic pattern. Also, the minimum values are not zero, as one would expect to see when an output SOP is orthogonal to the input SOP. The +1 diagonal shows an average half period of (24.25 ± 1.55)V while the −1 diagonal does not seem to have a constant period anymore with a half period ranging from (23 ± 1.55)V and (28 ± 1.55)V. This range of values reflects the curve's periodic nature starting to be lost.

4.1.3 First Run - Stage 3

For the third stage characterization, stages 1,2 and 4-6 had the datasheet bias voltages applied to account for the intrinsic birefringence. The circular

pattern was obtained by sweeping V_A and V_C within a [-80, 80]V range. The results obtained are graphically displayed in figure 4.5.

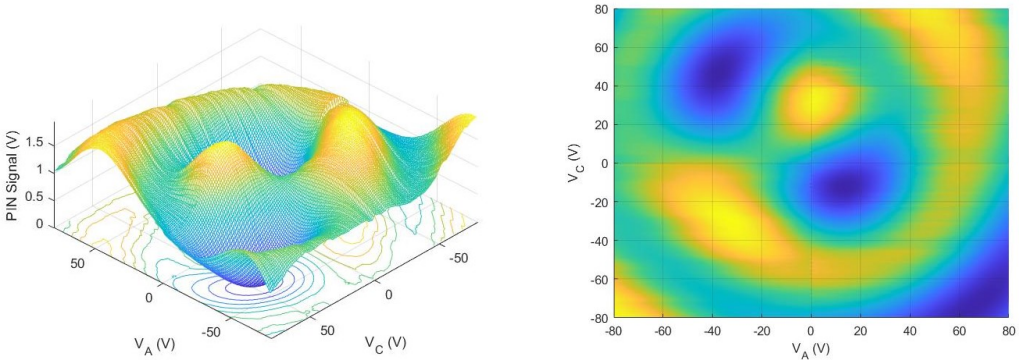

(a) (b)

Figure 4.5: Stage 3 PIN signal intensity when sweeping voltages V_A and V_C plotted a) in 3D with the contour plot underneath and b) as a 2D pattern

The Bias Point can be identified, but the first null starts to look less explicit. The elliptical pattern seems to be fading gradually, and the Bias Point starts merging with the ellipse of maximum intensity on the third quadrant. The -1 and $+1$ diagonals passing through the Bias Point, used to calculate the voltage parameters V_0 and V_π, are presented below.

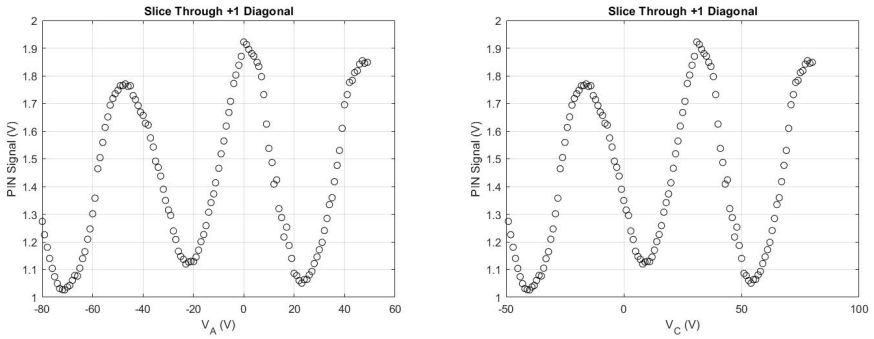

(a)

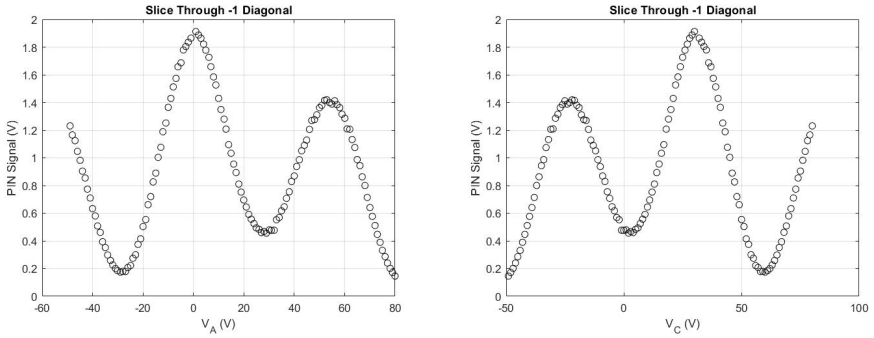

(b)

Figure 4.6: Stage 3 1D representation of the PIN signal plotted against each voltage individually where we have a) the +1 diagonal passing through the Bias Point and b) the −1 diagonal passing through the Bias Point

As expected from evaluating the 2D pattern, the peaks and valleys do not have the same intensity as in a perfect periodic pattern and are also starting to differ more between peers. Moreover, minimum values are farther away from zero, indicating that an orthogonal SOP at the output is not reached as intended. The +1 diagonal shows loss of periodicity with half period values ranging from 23V to 26V. Nevertheless, one calculated an average half period of (24.00 ± 1.55)V. The −1 diagonal looks smoother, but periodicity loss is still visible with a half period ranging from 25V to 30V, the average value being (27.50 ± 1.55)V.

4.1.4 First Run - Stage 4

For the fourth stage characterization, stages 1-3, 5 and 6 had the datasheet bias voltages applied to account for the intrinsic birefringence. The circular pattern was obtained by sweeping V_A and V_C within a [-80, 80]V range. The results obtained are graphically displayed in figure 4.7.

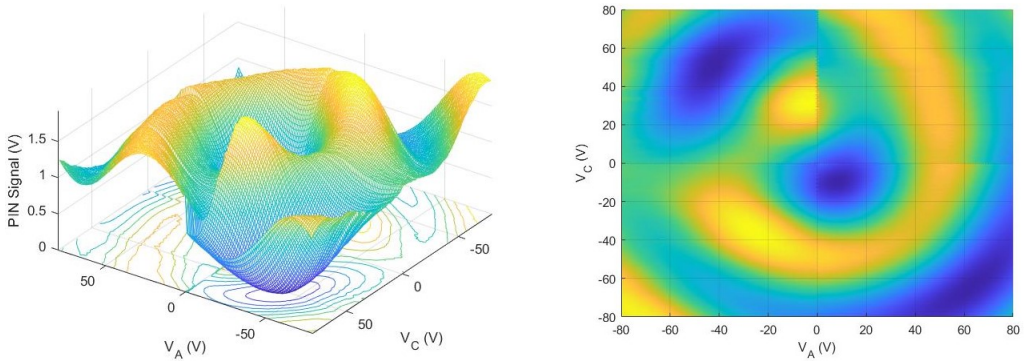

(a) (b)

Figure 4.7: Stage 4 PIN signal intensity when sweeping voltages V_A and V_C plotted a) in 3D with the contour plot underneath and b) as a 2D pattern

The Bias Point is still identifiable, but the first null starts vanishing as the ellipticity of the 2D pattern starts fading. The Bias Point starts merging with the ellipse of maximum intensity on the third quadrant. The -1 and $+1$ diagonals passing through the Bias Point, used to calculate the voltage parameters V_0 and V_π, are presented below.

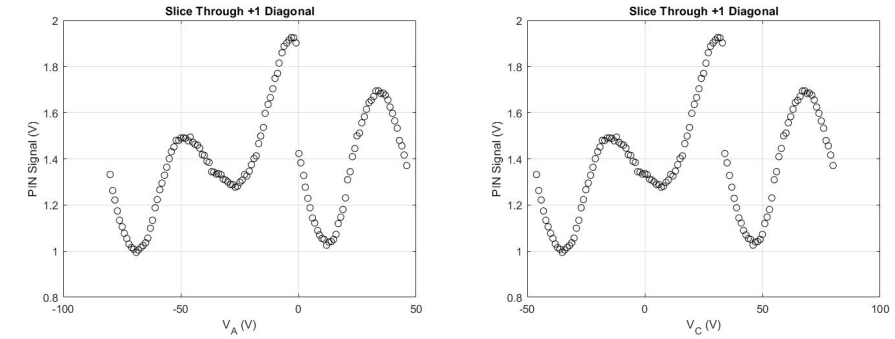

(a)

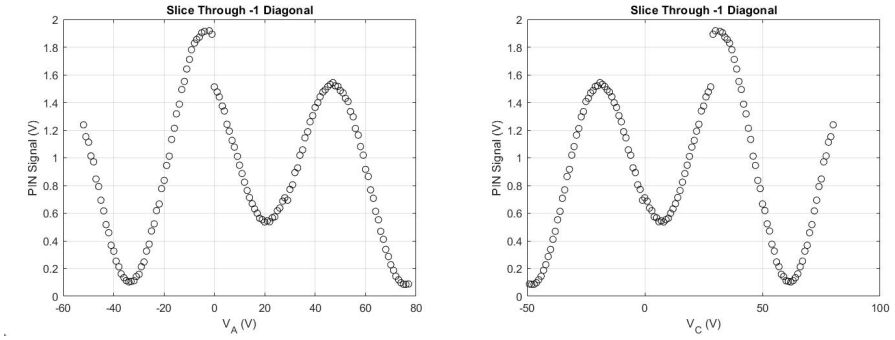

(b)

Figure 4.8: Stage 4 1D representation of the PIN signal plotted against each voltage individually where we have a) the +1 diagonal passing through the Bias Point and b) the −1 diagonal passing through the Bias Point

The diagonals are no longer close to a periodic wave with constant amplitude. Significant discrepancies in amplitude show that the output SOP is different from the expected, showing that the polarization state is not being maintained along the channel. Moreover, the period starts to be jeopardized, as one can assess from the +1 diagonal. Even though the −1 diagonal looks smooth, with half a period being in average (28.33 ± 1.55)V, the values still range from 26V to 30V.

4.1.5 First Run - Stage 5

For the fifth stage characterization, stages 1-4 and 6 had the datasheet bias voltages applied to account for the intrinsic birefringence. The circular pattern

was obtained by sweeping V_A and V_C within a [-80, 80]V range. The results obtained are graphically displayed in figure 4.9.

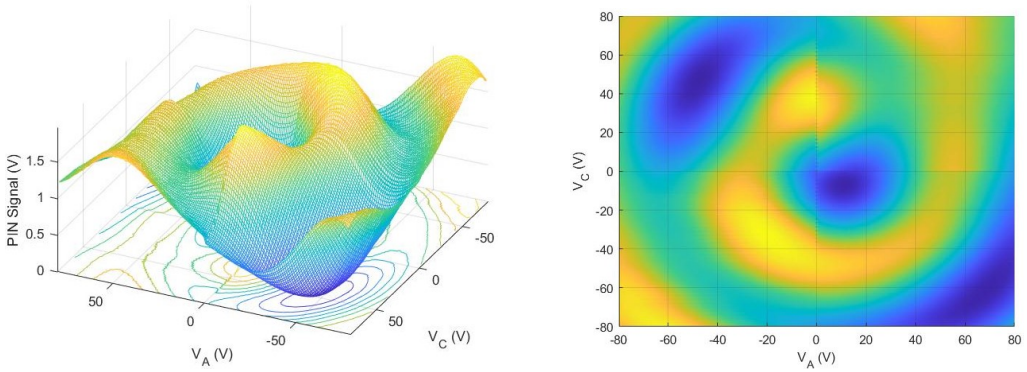

(a) (b)

Figure 4.9: Stage 5 PIN signal intensity when sweeping voltages V_A and V_C plotted a) in 3D with the contour plot underneath and b) as a 2D pattern

The graphical data starts to be more ambiguous, and the first null is no longer identifiable. In addition, what was seen as the Bias Point in the previous stages is now almost completely part of the outer ellipse, which is also losing shape. The -1 and $+1$ diagonals are traced as if the Bias Point was still the peak in the middle in an attempt to obtain voltage values that help calculate V_0 and V_π.

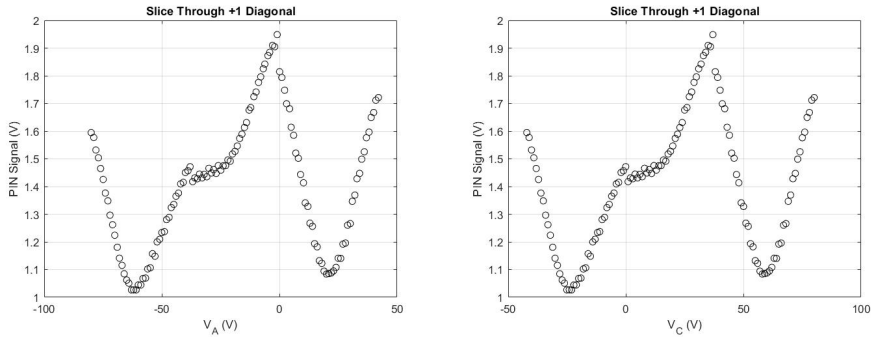

(a)

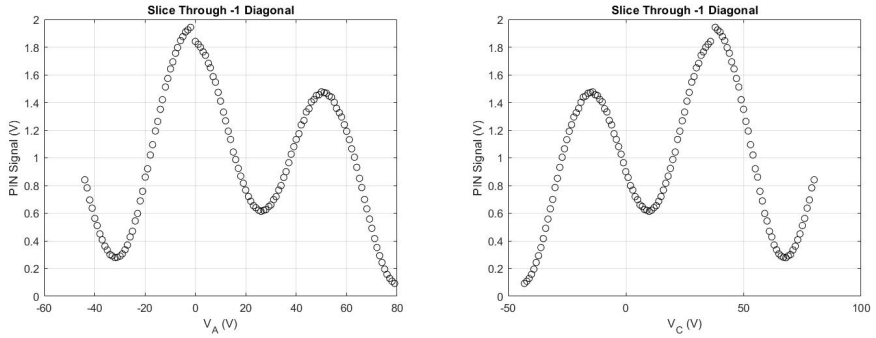

(b)

Figure 4.10: Stage 5 1D representation of the PIN signal plotted against each voltage individually where we have a) the +1 diagonal passing through the Bias Point and b) the −1 diagonal passing through the Bias Point

The +1 diagonal is no longer similar to a periodic wave with constant amplitude. Its minimums also show that an orthogonal output SOP is not even close to being reached in this particular direction. The −1 diagonal presents significant discrepancies in amplitude while also showing differences in aperture, having half periods ranging from 25V to 30V, with an average of 27.50±1.55V.

4.1.6 First Run - Stage 6

For the sixth stage characterization, stages 1-5 had the datasheet bias voltages applied to account for the intrinsic birefringence. The circular pattern was obtained by sweeping V_A and V_C within a [-80, 80]V range. The results obtained are graphically displayed in figure 4.11.

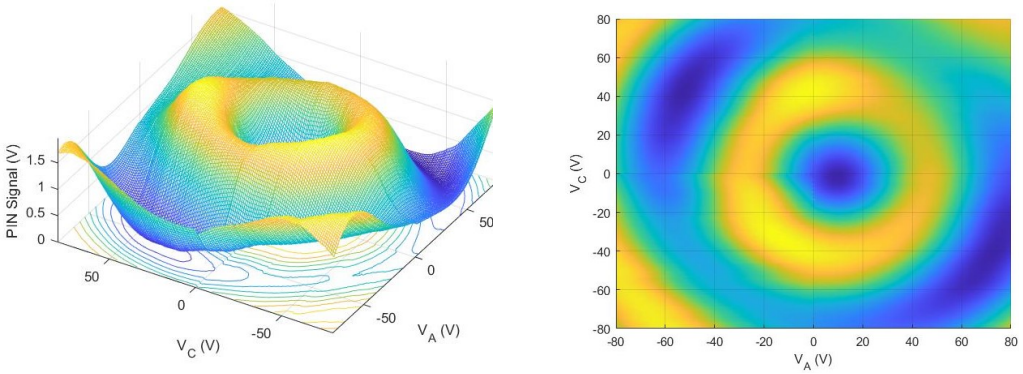

(a) (b)

Figure 4.11: Stage 6 PIN signal intensity when sweeping voltages V_A and V_C plotted a) in 3D with the contour plot underneath and b) as a 2D pattern

The pattern seems now to have changed entirely. In the 3D representation, one can recognize a valley where a peak is expected, and the first null seems to now be an ellipse of maximum intensity. Thus, the shift that was occurring in the previous stages became now evident. In this case, the -1 and $+1$ diagonals are not even worth tracing as one cannot be sure if the valley represents the Bias Point, which could jeopardize the calculation of the voltage parameters.

4.1.7 First Run - Data Analysis

Based on the data acquired in the first experimental run, the datasheet values are unreliable. Even though $LiNbO_3$ is not very susceptible to temperature changes, the temperature at which the parameters on the datasheet were obtained may have been different enough to make them unreliable to be used on calibration procedures. Moreover, the 2D pattern changes continuously as we advance from one stage to another, not giving much confidence in the data acquired. Therefore, better data should be retrieved by adjusting the method and employing different bias voltages. One hopes to achieve better results that can characterize the device and be compared to the datasheet values.

4.2 Second Data Acquisition - Switch Bias Voltages

In the second run of tests, the datasheet's bias voltages are applied only until they get replaced, which means the bias voltages obtained for the stages already tested will be utilized when characterizing the following ones. As the first stage would be tested only applying the datasheet's bias voltages, this stage is skipped, and the Bias Point from the first run of tests will be used.

An essential adaptation to the visualization method is made at this point. As one could see on the first acquisition, data gaps are recurrent due to hardware limitations. Therefore, for more accurate results, the voltage parameters will be calculated from the average half period of the diagonals when data gaps are an error source. This approach should minimize the error.

4.2.1 Second Run - Stage 2

For the second stage characterization, stages 3-6 had the datasheet bias voltages applied while stage 1 was set with $V_{A,Bias} = (-8.9 \pm 1.1)$V and $V_{C,Bias} = (21.0 \pm 1.1)$V. The circular pattern was obtained by sweeping V_A and V_C within a [-80, 80]V range. The results obtained are graphically displayed in figure 4.12.

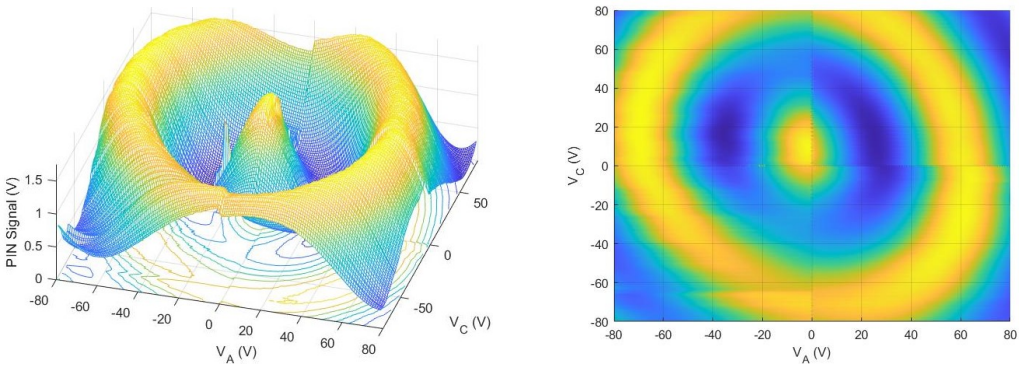

(a) (b)

Figure 4.12: Stage 2 PIN signal intensity when sweeping voltages V_A and V_C plotted a) in 3D with the contour plot underneath and b) as a 2D pattern

The graphical representation is very close to a perfect pattern. The first null does not have the same intensity all around but is well defined around the Bias Point. The -1 and $+1$ diagonals passing through the Bias Point, used to calculate the voltage parameters V_0 and V_π, are presented below.

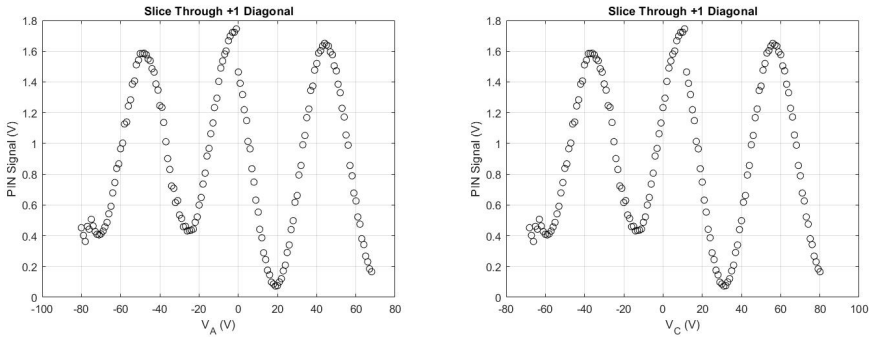

(a)

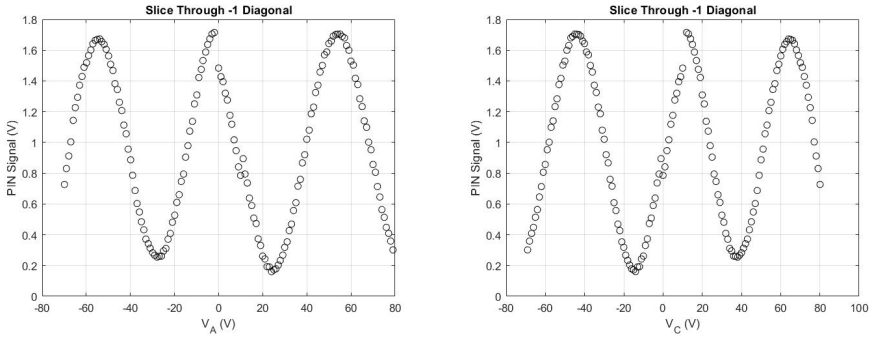

(b)

Figure 4.13: Stage 2 1D representation of the PIN signal plotted against each voltage individually where we have a) the +1 diagonal passing through the Bias Point and b) the −1 diagonal passing through the Bias Point

As one could assess from looking at the 2D pattern, the diagonals are fairly good. The +1 and −1 diagonals have approximately a half period of (23.50 ± 1.55)V and (27.17 ± 1.55)V, respectively. However, amplitude variations are already noticeable, possibly due to the birefringence along the channel, which changes the desired output SOP.

4.2.2 Second Run - Stage 3

For the third stage characterization, stages 4-6 had the datasheet bias voltages applied while stage 1 was set with $V_{A,Bias} = (-8.9 \pm 1.1)$V and $V_{C,Bias} = (21.0 \pm 1.1)$V, and stage 2 with $V_{A,Bias} = (-1.0 \pm 1.1)$V and $V_{C,Bias} = (11.0 \pm 1.1)$V. The circular pattern was obtained by sweeping V_A and V_C within a [-80, 80]V range. The results obtained are graphically displayed in figure 4.14.

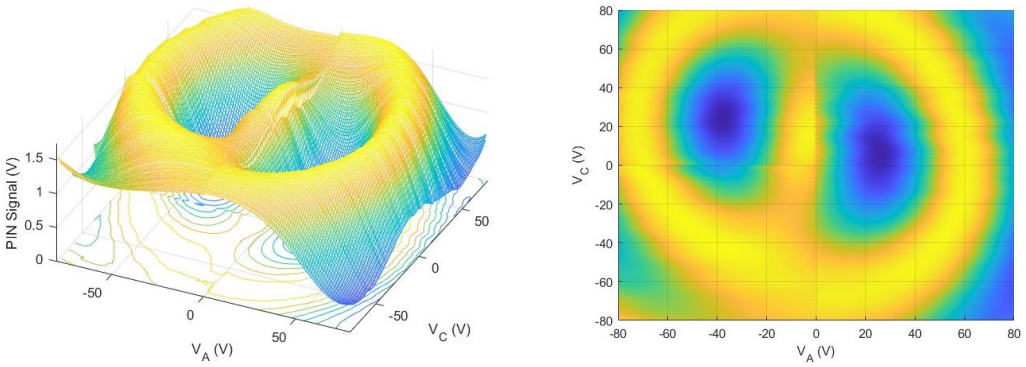

(a) (b)

Figure 4.14: Stage 3 PIN signal intensity when sweeping voltages V_A and V_C plotted a) in 3D with the contour plot underneath and b) as a 2D pattern

The graphical representation shows that the first null is not well defined as the Bias Point is connected to the ellipse of maximum intensity. Nevertheless, the pattern still resembles an ellipse. The -1 and $+1$ diagonals passing through the Bias Point (considered the point of maximum intensity despite the poor definition), used to calculate the voltage parameters V_0 and V_π, are presented below.

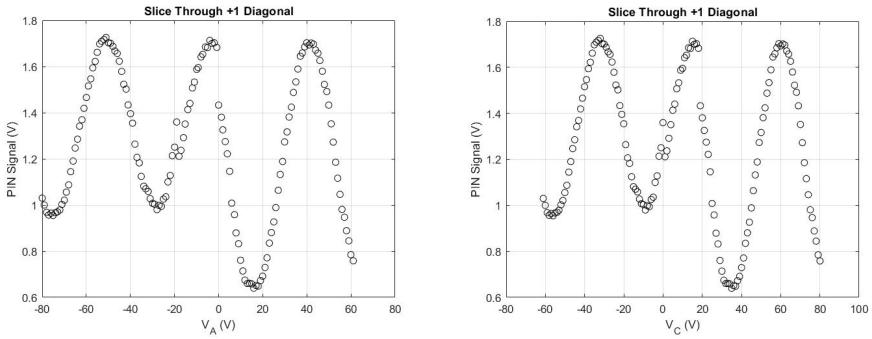

(a)

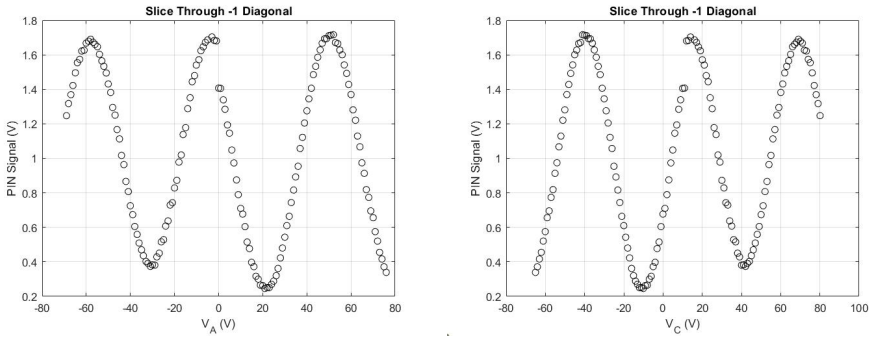

(b)

Figure 4.15: Stage 3 1D representation of the PIN signal plotted against each voltage individually where we have a) the +1 diagonal passing through the Bias Point and b) the −1 diagonal passing through the Bias Point

Even though the 2D pattern was not the best, the diagonals are good enough to look periodic. The +1 and −1 diagonals have an average half period of (24.00± 1.55)V and (28.00 ± 1.55)V, respectively. However, amplitude variations are a major factor already, as one could expect from the fact that the first null is poorly defined. Once again, the wanted pattern was not obtained, which will probably cause a deviation when calculating the voltage parameters V_0 and V_π.

4.2.3 Second Run - Stage 4

For the fourth stage characterization, stages 5 and 6 had the datasheet bias voltages applied while the other stages had the following bias voltages:

	Stage 1	**Stage 2**	**Stage 3**
$V_{A,Bias}$ (V)	-8.9±1.1	-1.0±1.1	-4.0±1.1
$V_{C,Bias}$ (V)	21.0±1.1	11.0±1.1	15.0±1.1

Table 4.2: Bias Voltages obtained for the stages already tested, applied in substitution of the given datasheet values

The circular pattern was obtained by sweeping V_A and V_C within a [-80, 80]V range. The results obtained are graphically displayed in figure 4.16.

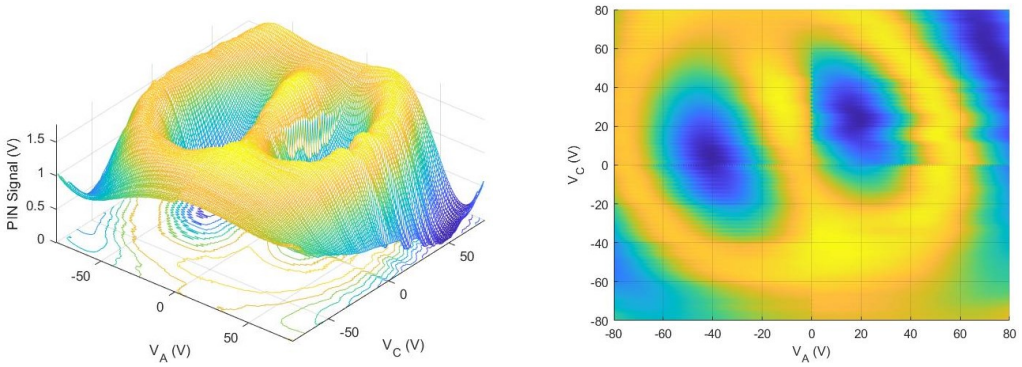

(a) (b)

Figure 4.16: Stage 4 PIN signal intensity when sweeping voltages V_A and V_C plotted a) in 3D with the contour plot underneath and b) as a 2D pattern

Just like for stage 3, the graphical representation shows that the first null is not well defined as the Bias Point is connected to the ellipse of maximum intensity. Once again, the pattern still resembles an ellipse. The -1 and $+1$ diagonals passing through the Bias Point (considered the point of maximum intensity despite poor definition), used to calculate the voltage parameters V_0 and V_π, are presented below.

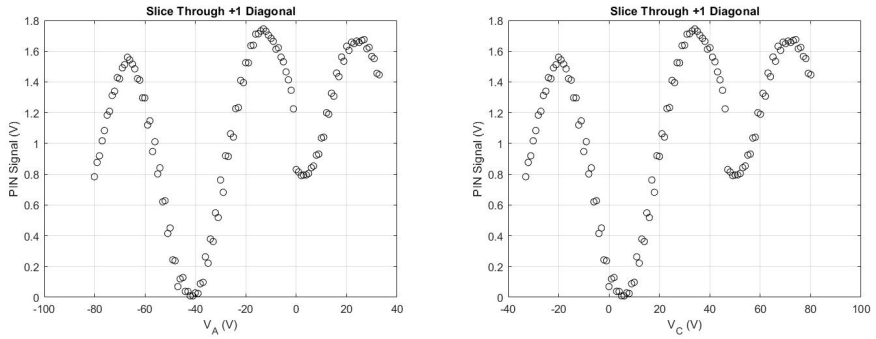

(a)

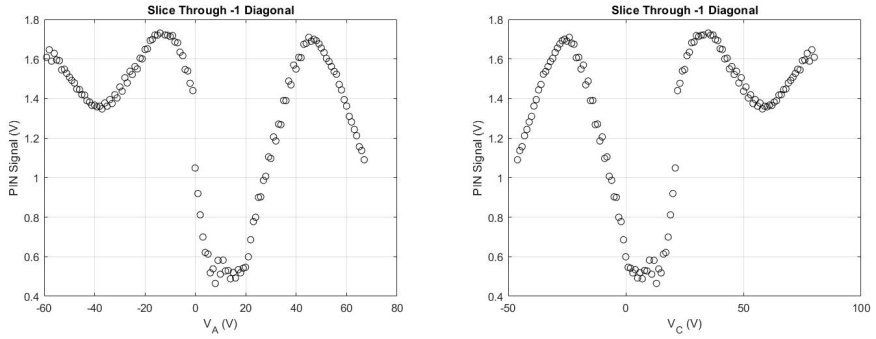

(b)

Figure 4.17: Stage 4 1D representation of the PIN signal plotted against each voltage individually where we have a) the +1 diagonal passing through the Bias Point and b) the −1 diagonal passing through the Bias Point

The diagonals are not good at all. First, there is distortion in the data caused by some exterior interference on the system affecting both diagonals. Secondly, the changes in amplitude are massive. Finally, the curves are not periodic at all. For example, on the +1 diagonal, the data to the left of the gap shows an average half period of (28 ± 1.55)V, as to the right, it is of just (22 ± 1.55)V. Nevertheless, an average half period was calculated, being (25.17 ± 1.55)V. Moreover, the −1 diagonal is just as bad, and the change in aperture is easily noticeable. The voltage parameter V_π will not be calculated using the average half period in this case, being more accurate to obtain it visually from the 2D pattern.

4.2.4 Second Run - Stage 5

For the fifth stage characterization, stage 6 had the datasheet bias voltages applied while the other stages had the following bias voltages applied:

	Stage 1	**Stage 2**	**Stage 3**	**Stage 4**
$V_{A,Bias}$ (V)	-8.9±1.1	-1.0±1.1	-4.0±1.1	-13.0±1.1
$V_{C,Bias}$ (V)	21.0±1.1	11.0±1.1	15.0±1.1	30.0±1.1

Table 4.3: Bias Voltages obtained for the stages already tested, applied in substitution of the given datasheet values

The circular pattern was obtained by sweeping V_A and V_C within a [-80, 80]V range. The results obtained are graphically displayed in figure 4.18.

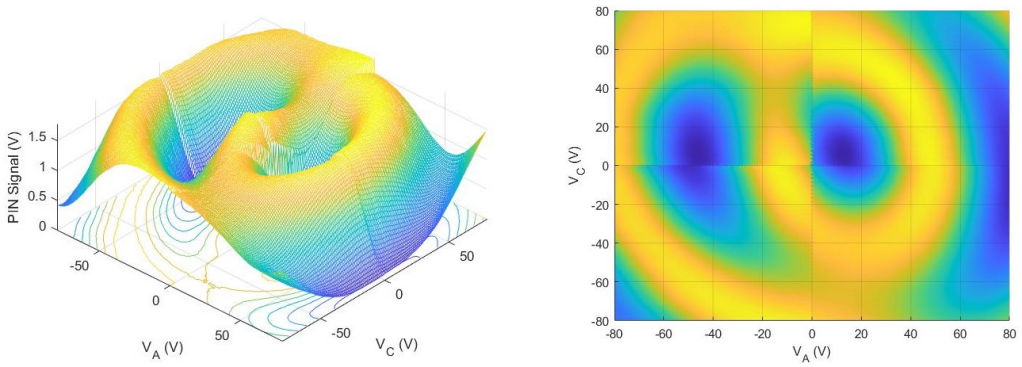

(a) (b)

Figure 4.18: Stage 5 PIN signal intensity when sweeping voltages V_A and V_C plotted a) in 3D with the contour plot underneath and b) as a 2D pattern

Like in the previous two stages, the graphical representation shows that the first null is not well defined as the Bias Point is connected to the ellipse of maximum intensity. Moreover, the elliptical pattern is starting to disappear. This pattern change is very similar to what happened in the first run of tests. Nevertheless, one must still watch what happens with the last stage to assess if the elliptical shape changes completely or if a better result is obtained. The

-1 and $+1$ diagonals passing through the Bias Point (considered the point of maximum intensity despite poor definition), used to calculate the voltage parameters V_0 and V_π, are presented below.

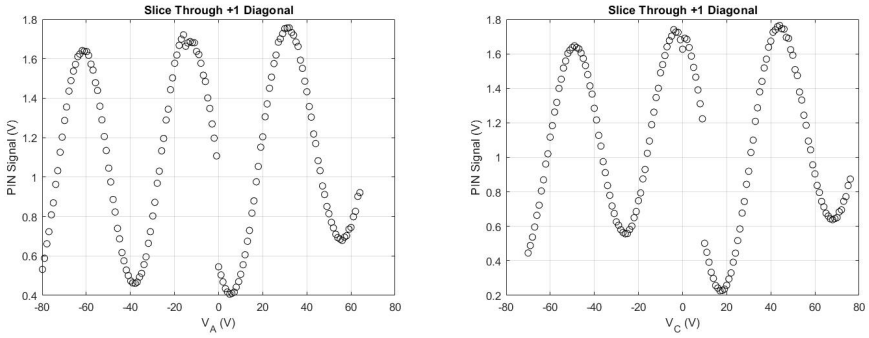

(a)

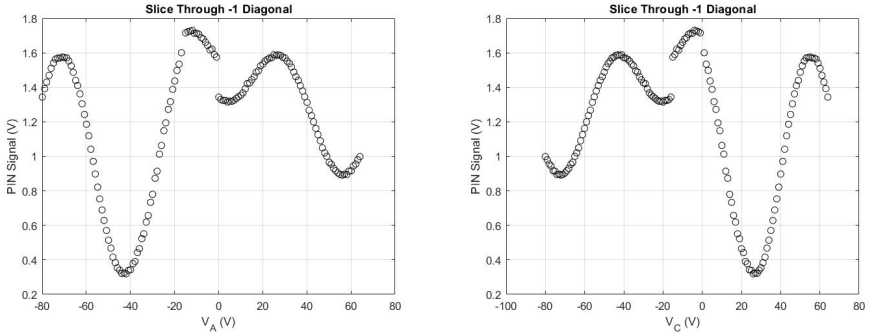

(b)

Figure 4.19: Stage 5 1D representation of the PIN signal plotted against each voltage individually where we have a) the $+1$ diagonal passing through the Bias Point and b) the -1 diagonal passing through the Bias Point

The $+1$ diagonal is reasonably periodic, with an average half period of (24.67 ± 1.55)V, even though data gaps continue to occur around the same zone ($V_A = 0$) due to the hardware constraints. On the other hand, the -1 diagonal has no regular period or amplitude, with half periods ranging from 22V to 30V.

4.2.5 Second Run - Stage 6

Finally, for the sixth stage characterization, the bias voltages applied to stages 1-5 were the following:

	Stage 1	**Stage 2**	**Stage 3**	**Stage 4**	**Stage 5**
$V_{A,Bias}$ (V)	-8.9±1.1	-1.0±1.1	-4.0±1.1	-13.0±1.1	-13.9±1.1
$V_{C,Bias}$ (V)	21.0±1.1	11.0±1.1	15.0 ±1.1	30.0±1.1	-4.0±1.1

Table 4.4: Bias Voltages obtained for the stages already tested, applied in substitution of the given datasheet values

The circular pattern was obtained by sweeping V_A and V_C within a [-80, 80]V range. The results obtained are graphically displayed in figure 4.20.

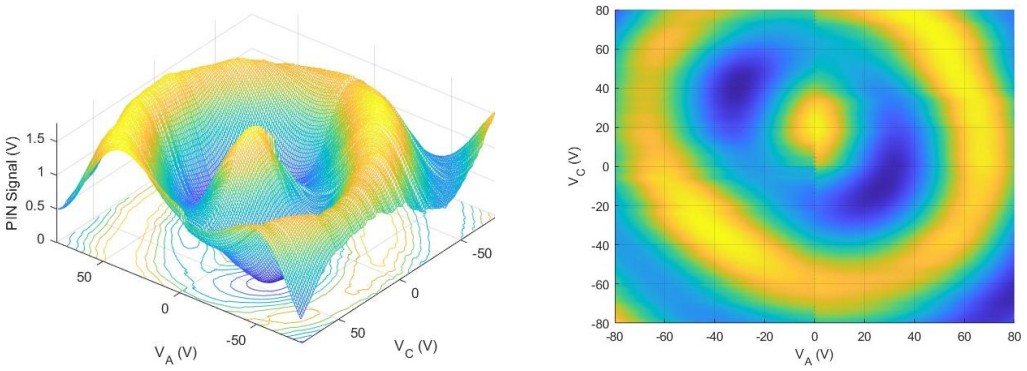

(a) (b)

Figure 4.20: Stage 6 PIN signal intensity when sweeping voltages V_A and V_C plotted a) in 3D with the contour plot underneath and b) as a 2D pattern

For the last stage, the graphical representation shows a much better elliptical pattern, where the first null is not perfect but still well defined around the Bias Point, which is no longer connected to the maximum intensity ellipse. The -1 and $+1$ diagonals passing through the Bias Point, used to calculate the voltage parameters V_0 and V_π, are presented below.

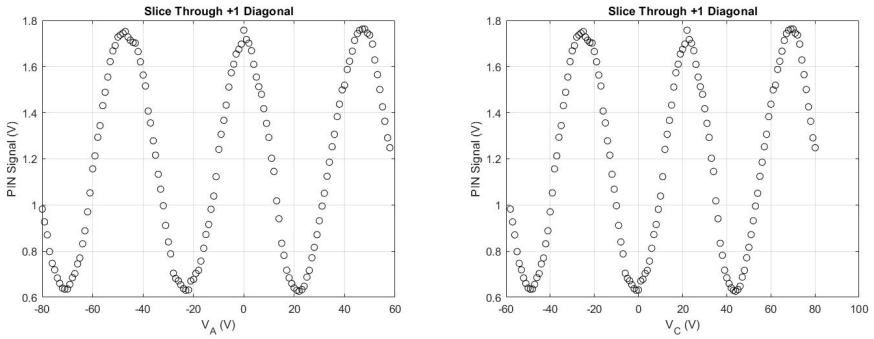

(a)

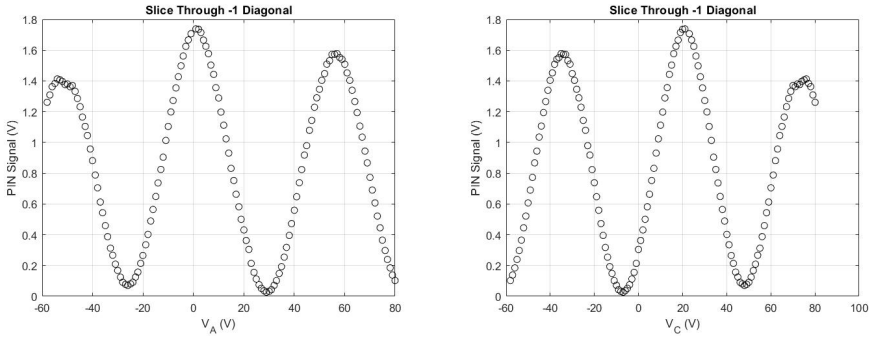

(b)

Figure 4.21: Stage 6 1D representation of the PIN signal plotted against each voltage individually where we have a) the +1 diagonal passing through the Bias Point and b) the −1 diagonal passing through the Bias Point

As expected by observing the 2D pattern, the diagonals are reasonably periodic with the +1 and −1 diagonals having average half periods of (24.33 ± 1.55)V and (27.12±1.55)V, respectively. The amplitude of the +1 diagonal is constant, but the minimum value does not near zero. In the −1 diagonal, the amplitude has some fluctuations, but it comes much closer to zero on the minimums.

4.2.6 Second Run - Data Analysis

The data acquired with the bias voltage adjustment was somewhat better, making it possible to identify a Bias Point, or close to it, for all stages. Consequently, one used this data set to calculate the voltage parameters using the graphical visualization method, followed by calculating the intrinsic parameters. These were then used to make a theoretical display of the 2D pattern.

The datasheet parameters are presented on table 4.5

	Stage 1	**Stage 2**	**Stage 3**	**Stage 4**	**Stage 5**	**Stage 6**
$V_{A,Bias}$ (V)	-10.7	-9.3	-8.5	-10.9	-7.4	-7.6
$V_{C,Bias}$ (V)	8.4	9.6	9.4	11.1	11.6	10.9
V_0	27.2	27	27	26.9	26.8	27.2
V_π	56.3	56	55.9	56.1	56.1	56
t_{11}	0.1156	0.1165	0.1163	0.1169	0.1172	0.1154
t_{12}	0	0	0	0	0	0
t_{21}	0.02	0.0199	0.0216	0.02	0.02	0.0212
t_{22}	0.0558	0.0561	0.0562	0.056	0.056	0.0561
t_{1i}	0.1358	-0.0184	-0.0564	-0.0088	-0.2467	-0.1901
t_{2i}	1.0881	1.0598	0.9976	1.2309	1.0247	1.0075

Table 4.5: Datasheet values for each stage's characterization

The calculated parameters for the 6-stage EPC in this test run are displayed on table 4.6.

	Stage 1	**Stage 2**	**Stage 3**	**Stage 4**	**Stage 5**	**Stage 6**
$V_{A,Bias}$ (V)	-8.9±1.1	-1.0±1.1	-4.0±1.1	-13.0±1.1	-13.9±1.1	1.0±1.1
$V_{C,Bias}$ (V)	21.0±1.1	11.0±1.1	15.0±1.1	30.0±1.1	-4.0±1.1	21.0±1.1
V_0	24.8	23.5	24.0	25.2	24.7	24.3
V_π	56.0	54.9	55.9	50.0	62.0	54.9
t_{11}	-0.1264	-0.1337	-0.1309	-0.1194	-0.1224	-0.1348
t_{12}	0.0009	0.0001	-0.0001	-0.0207	-0.0021	0
t_{21}	0.0002	0	0	0.0111	0.0041	0.0050
t_{22}	0.0571	0.0583	0.0583	0.0746	0.0525	0.0582
t_{1i}	0.7923	0.6669	0.7176	0.1236	-1.1168	1.4832
t_{2i}	1.7064	0.6994	1.1074	3.1156	0.5565	1.1086

Table 4.6: Parameters characterizing each stage for the data retrieved in the 2nd test run

Compared to the patterns obtained in the first run of tests, the results were improved enough to characterize the EPC. Nevertheless, the acquired intrinsic parameters are very different from the datasheet values for certain stages.

First, all bias voltages are different, and in stages 5 and 6, a change in signal occurs. Second, the voltage parameter V_0 was overall inferior but relatively constant through all stages. On the other hand, the values for V_π were very similar to the datasheet ones, except for stages 4 and 5, where the -1 diagonal was not periodic. The intrinsic parameters calculated were close to expected, but again, some outliers arose. Overall, the discrepancies are due to the patterns not being perfect, with wider gaps happening for the stages where one got worse outcomes. The mathematical formulation was employed to see the perfect pattern if these parameters were correct. Figure 4.22 shows these graphics. Note that these do not characterize the EPC, only validating the mathematical model and evaluating the similarity of the acquired parameters to what one should expect.

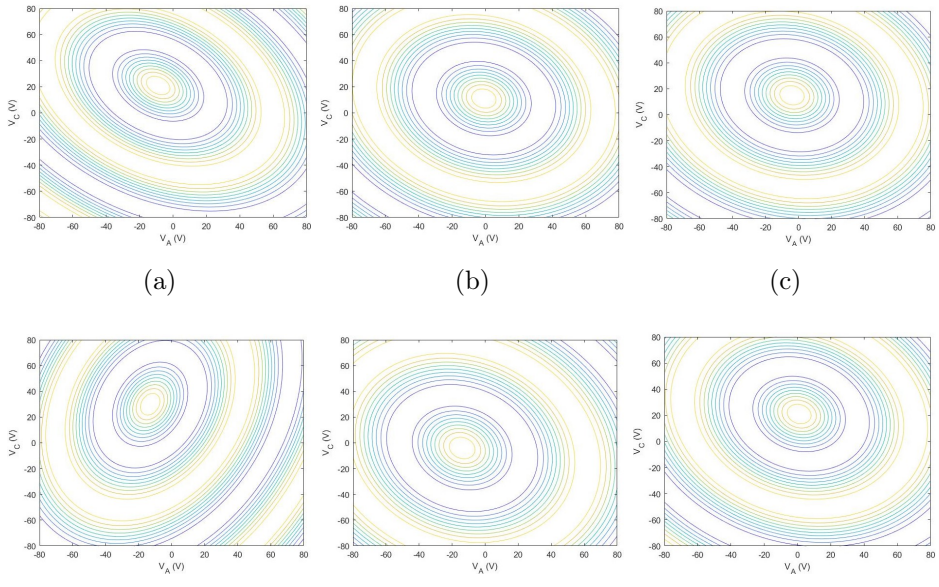

Figure 4.22: Representation of the 2D pattern, constructed by employing the mathematical formulation for a) stage 1; b) stage 2; c) stage 3; d) stage 4; e) stage 5 and f) stage 6

From the above ellipses, one can see how the apertures and orientation vary. If the parameters were correct, the graphics should be more alike in orientation and period, with the main difference being the Bias Point. From the data above, one can conclude that the bias voltages are still not correct. Another approximation attempt was made with hopes of better results.

4.3 Third Data Acquisition - Improvement Attempt

In the third run of tests, the bias voltages displayed on table 4.6 are applied on the stages not yet tested, being substituted once new values are obtained. This time, the 2D patterns are displayed side by side in figure 4.23.

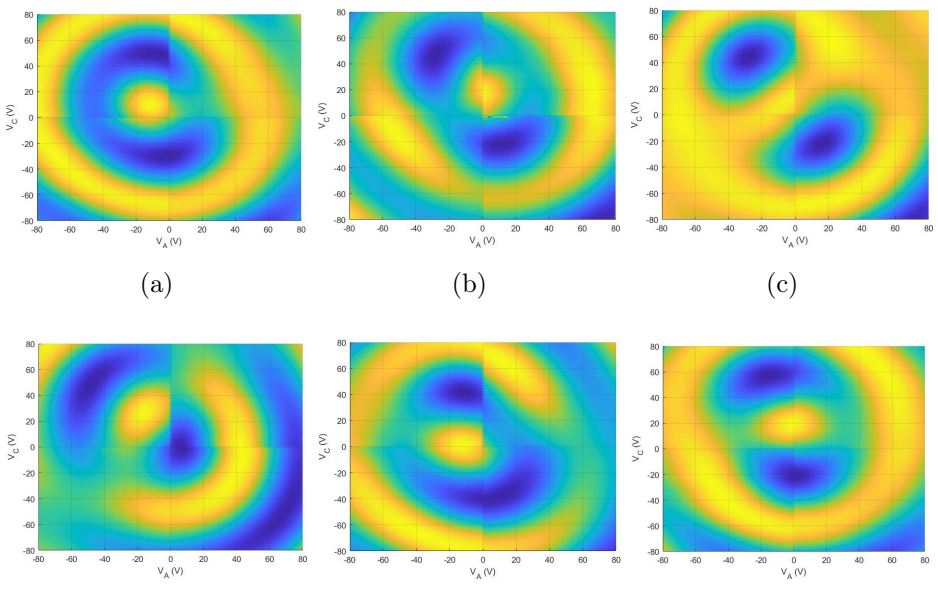

Figure 4.23: Obtained 2D pattern in the 3rd run of tests for a) stage 1; b) stage 2; c) stage 3; d) stage 4; e) stage 5 and f) stage 6

The 2D representations show that the ellipticity is evident in most stages, but it is unclear if better parameters can be extracted from the pattern. The first null did not get perfectly defined in any stage, gaps occur on the ellipse

of maximum intensity in stages 4 and 5, and stage 3 still does shows poor definition of the Bias Point. The approach taken in the second run of tests was replicated to calculate the characterizing parameters. These are presented in the table below.

	Stage 1	**Stage 2**	**Stage 3**	**Stage 4**	**Stage 5**	**Stage 6**
$V_{A,Bias}$ (V)	-12.0±1.1	1.0±1.1	-5.0±1.1	-14.1±1.1	-11.9±1.1	-1.0±1.1
$V_{C,Bias}$ (V)	10.0±1.1	17.0±1.1	10.0±1.1	29.0±1.1	1.0±1.1	18.0±1.1
V_0	25.3	24.5	24.1	25.0	24.1	26.0
V_π	54.0	54.0	55.9	55.8	53.8	56.0
t_{11}	-0.1242	-0.1282	-0.1304	-0.1257	-0.1277	-0.1211
t_{12}	0.0011	0.0010	-0.0002	-0.0002	-0.0001	-0.0001
t_{21}	0	0	0	0	0.0024	0.0002
t_{22}	0.0594	0.0533	0.0561	0.0563	0.0583	0.0543
t_{1i}	-0.1009	1.1697	0.3224	0.9265	-0.6976	1.0271
t_{2i}	1.3065	0.8534	0.8415	2.4266	0.7648	1.0291

Table 4.7: Parameters characterizing each stage for the data retrieved in the 3rd test run

The parameters above were employed to build the theoretical patterns comparable to the graphical representations in figure 4.23.

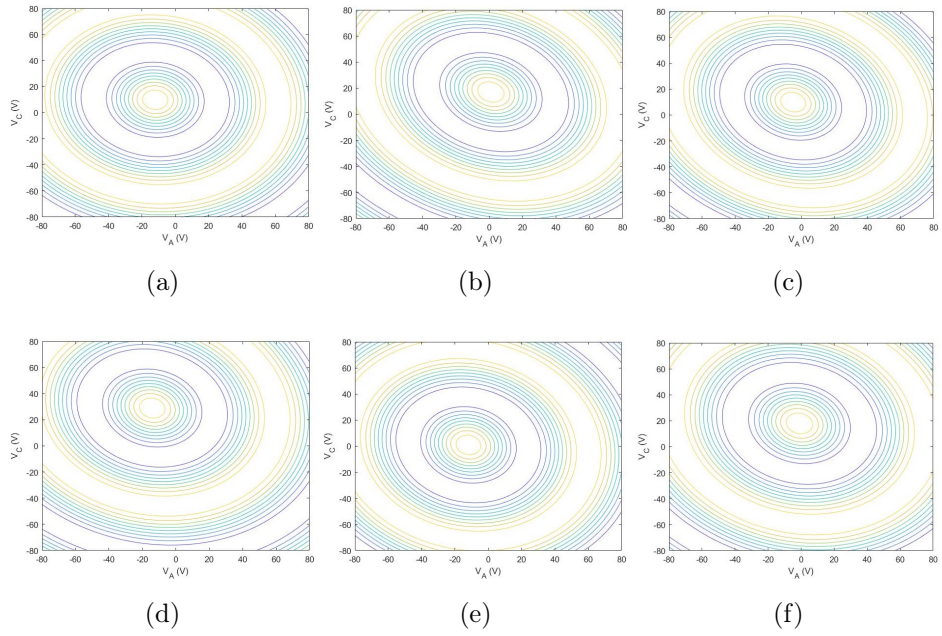

Figure 4.24: Theoretical 2D patterns constructed using the parameters obtained in the 3rd run of tests for a) stage 1; b) stage 2; c) stage 3; d) stage 4; e) stage 5 and f) stage 6

Overall, the parameters show minor fluctuations comparing to the second run, with drastic improvements in stages 4 and 5. The theoretical patterns reinforce precisely that, with the displayed graphics much closer to each other in orientation and periodicity. Even so, one must acknowledge that the approximations employed using average half periods for worse patterns have a significant impact on this approximation. After evaluating the new data, one is not assured that continuing this process will lead to good enough results, applicable to characterize the EPC rightfully. For characterization purposes, the big picture still shows the struggle in achieving perfectly periodic patterns, corresponding to the challenge of establishing a circular SOP both at the input and output of the EPC. Moreover, accurate bias voltages are essential in maintaining a steady SOP along the channel. Deviations in these values due to power supply limitations, using SMF and not automatically controlling the input and output SOP in real time lead to errors that extend from one stage to the other.

Chapter 5

Conclusion

5.1 Concluding Thoughts

This work was organized into three different components. First, the study of DV-QKD systems and polarization modelling was fulfilled, focusing on electro-optic polarization controllers. Secondly, a mathematical model of the EOSPACE EPC was accomplished so its functionality was easily expressed and its posterior characterization possible. Finally, a characterizing method was proposed as an adaptation of the one used by EOSPACE. This stage involved PLC remote control, automation of the whole process and data acquisition.

The software to accomplish this method needs to control the SOP at both the input and output with real time graphical display. This capability is necessary to adjust the data and obtain a perfect periodic 2D pattern. However, by establishing a fixed input and trying to achieve a close enough pattern, perfect characterization is not achievable due to hardware and environmental constraints causing the polarization to drift along the channel. Moreover, the data could only be graphically displayed after all the data points were acquired, which means getting PIN intensity values for a 161×161 matrix of values when using a 1V step.

Hardware is also a critical part of the process. The power supplies used had a hard time decreasing voltages due to their capacitors' discharge being very slow near 0V. The characterization process employing a 1V step would take two and a half hours for each stage due to this constraint. The time was reduced to one hour and forty minutes by using two 15kΩ resistors to accelerate the capacitors discharge. Still, the method takes too much time, and reducing the step for more accurate results would not be reasonable.

The fact that sensitive components are used when maintaining a specific SOP with no active control is also a problem. The SMF was stretched and taped over the laboratory counter to minimize any mechanical errors, but the system requires calibration as polarization drift happens over time.

To conclude, the method used does not show the capability to be employed in the laboratory. Calibration procedures require a suitable characterization method. It should be fast enough to be efficiently employed before using the device in a DV-QKD system, guaranteeing that the characterizing parameters are still reliable when the EPC is used. Moreover, the acquired parameters need to be objectively correct, otherwise, the results obtained when using the device in a transmission system will be faulty.

5.2 Future Work

The method employed throughout this work should not be used in future applications as it shows many constraints and no practical use in future transmitter integration. Instead, a solution using real-time SOP control and analysis should be pursued using the capabilities of a polarimeter at the EPC output. Moreover, this solution should not depend on a specific input SOP as maintaining it over the communicating channel is not feasible when SMF fibre is utilized. After a reliable characterization method is found, the EPC fast SOP control can be examined for posterior transmitter implementation.

Bibliography

[1] Feihu Xu, Xiongfeng Ma, Qiang Zhang, Hoi-Kwong Lo, and Jian-Wei Pan. Secure quantum key distribution with realistic devices. *Rev. Mod. Phys.*, 92:025002, May 2020.

[2] Eleni Diamanti, Hoi Kwong Lo, Bing Qi, and Zhiliang Yuan. Practical challenges in quantum key distribution. *npj Quantum Information*, 2(1):1–12, 2016.

[3] Peter W. Shor. Polynomial-time algorithms for prime factorization and discrete logarithms on a quantum computer. *SIAM Journal on Computing*, 26(5):1484–1509, 1997.

[4] Chi Cheng, Rongxing Lu, Albrecht Petzoldt, and Tsuyoshi Takagi. Securing the internet of things in a quantum world. *IEEE Communications Magazine*, 55(2):116–120, 2017.

[5] Jack D. Hidary. *A Brief History of Quantum Computing*, pages 11–16. Springer International Publishing, Cham, 2019.

[6] Nicolas Gisin, Grégoire Ribordy, Wolfgang Tittel, and Hugo Zbinden. Quantum cryptography. *Reviews of Modern Physics*, 74(1):145–195, 2002.

[7] Ivan B. Djordjevic. *Quantum-Key Distribution (QKD) Fundamentals*, pages 211–265. Springer International Publishing, Cham, 2019.

[8] Michael A. Nielsen and Isaac L. Chuang. *Quantum Computation and Quantum Information*. Cambridge University Press, 2000.

[9] A. Duplinskiy, V. Ustimchik, A. Kanapin, V. Kurochkin, and Y. Kurochkin. Low loss QKD optical scheme for fast polarization encoding. *arXiv*, 25(23):28886–28897, 2017.

[10] Dimitris Giampouris. Short review on quantum key distribution protocols. *Advances in Experimental Medicine and Biology*, 988:149–157, 2017.

[11] Zhao Yue Dong, Ning Na Yu, Zheng Jun Wei, Jin Dong Wang, and Zhi Ming Zhang. An attack aimed at active phase compensation in one-way phase-encoded QKD systems. *European Physical Journal D*, 68(8):0–5, 2014.

[12] Alan Kanapin, Alexander Duplinskiy, Alexander Sokolov, Sergey Vorobey, Alexander Miller, Vladimir Kurochkin, and Yury Kurochkin. Urban QKD test for phase and polarization encoding devices. *International Journal of Quantum Information*, 15(8):1–9, 2017.

[13] Matthias Scholz, Nils Neubauer, and Oliver Benson. Time-bin encoding for narrow-band single photons. *2008 Conference on Quantum Electronics and Laser Science Conference on Lasers and Electro-Optics, CLEO/QELS*, pages 9–10, 2008.

[14] Lijun Ma, Tiejun Chang, Alan Mink, Slattery Slattery, Barry Hershman, and Xiao Tang. Experimental demonstration of a detection-time-bin-shift polarization encoding quantum key distribution system. *IEEE Communications Letters*, 12(6):459–461, 2008.

[15] W. K. Wootters and W. H. Zurek. A single quantum cannot be cloned. *Nature*, 299(5886):802–803, October 1982.

[16] S. Pirandola, U. L. Andersen, L. Banchi, M. Berta, D. Bunandar, R. Colbeck, D. Englund, T. Gehring, C. Lupo, C. Ottaviani, J. Pereira, M. Razavi, J. S. Shaari, M. Tomamichel, V. C. Usenko, G. Vallone, P. Villoresi, and P. Wallden. Advances in quantum cryptography. *arXiv*, pages 8–15, 2019.

[17] Dagmar Bruß. Optimal eavesdropping in quantum cryptography with six states. *Phys. Rev. Lett.*, 81:3018–3021, Oct 1998.

[18] Valerio Scarani, Antonio Acín, Grégoire Ribordy, and Nicolas Gisin. Quantum Cryptography Protocols Robust against Photon Number Splitting Attacks for Weak Laser Pulse Implementations. *Physical Review Letters*, 92(5):4, 2004.

[19] Norbert Lütkenhaus. Security against individual attacks for realistic quantum key distribution. *Physical Review A - Atomic, Molecular, and Optical Physics*, 61(5):10, 2000.

[20] Misael Caloz, Matthieu Perrenoud, Claire Autebert, Boris Korzh, Markus Weiss, Christian Schönenberger, Richard J. Warburton, Hugo Zbinden, and Félix Bussières. High-detection efficiency and low-timing jitter with amorphous superconducting nanowire single-photon detectors. *Applied Physics Letters*, 112(6), 2018.

[21] Iman Esmaeil Zadeh, Johannes W.N. Los, Ronan B.M. Gourgues, Violette Steinmetz, Gabriele Bulgarini, Sergiy M. Dobrovolskiy, Val Zwiller, and Sander N. Dorenbos. Single-photon detectors combining high efficiency, high detection rates, and ultra-high timing resolution. *APL Photonics*, 2(11), 2017.

[22] J. P. Gordon and H. Kogelnik. PMD fundamentals: Polarization mode dispersion in optical fibers. *Proceedings of the National Academy of Sciences of the United States of America*, 97(9):4541–4550, 2000.

[23] Misha Brodsky, Nicholas J. Frigo, Misha Boroditsky, and Moshe Tur. Polarization mode dispersion of installed fibers. *Journal of Lightwave Technology*, 24(12):4584–4599, 2006.

[24] P.K.A. Wai and C.R. Menyak. Polarization mode dispersion, decorrelation, and diffusion in optical fibers with randomly varying birefringence. *Journal of Lightwave Technology*, 14(2):148–157, 1996.

[25] H. J. Briegel, W. Dür, J. I. Cirac, and P. Zoller. Quantum repeaters: The role of imperfect local operations in quantum communication. *Physical Review Letters*, 81(26):5932–5935, 1998.

[26] Suwat Thaniyavarn. Wavelength-independent, optical-damage-immune linbo3 te–tm mode converter. *Opt. Lett.*, 11(1):39–41, Jan 1986.

[27] Costantino Agnesi, Marco Avesani, Andrea Stanco, Paolo Villoresi, and Giuseppe Vallone. All-fiber self-compensating polarization encoder for quantum key distribution. *Optics Letters*, 44(10):2398, may 2019.

[28] Marco Avesani, Costantino Agnesi, Andrea Stanco, Giuseppe Vallone, and Paolo Villoresi. Stable, low-error and calibration-free polarization encoder for free-space quantum communication. *arXiv*, 45(17):4706–4709, 2020.

[29] Grant R Fowles. *Introduction to modern optics / Grant R. Fowles.* Holt, Rinehart and Winston, New York, 2d ed. edition, 1975.

[30] Dennis H Goldstein. *Polarized light*. CRC press, 2017.

[31] J.N. Damask. *Polarization Optics in Telecommunications*. Springer Series in Optical Sciences. Springer, 2004.

[32] R.M.A. Azzam, N.M. Bashara, and N.M. Bashara. *Ellipsometry and Polarized Light*. Ballard CREOL collection. North-Holland Publishing Company, 1977.

[33] William H McMaster. Polarization and the stokes parameters. *American Journal of Physics*, 22(6):351–362, 1954.

[34] Soe-Mie F Nee. Polarization measurement. In *Measurement, Instrumentation, and Sensors Handbook*, pages 49–1. CRC Press, 2017.

[35] Dan C. Marinescu and Gabriela M. Marinescu. Chapter 6 - physical realization of quantum information processing systems. In Dan C. Marinescu and Gabriela M. Marinescu, editors, *Classical and Quantum Information*, pages 563–649. Academic Press, Boston, 2012.

[36] F.A. Jenkins, H.E. White, and joint author White. *Fundamentals of Optics*. International student edition. McGraw-Hill, 1976.

[37] Arjan JP van Haasteren, Jos JGM van der Tol, M Oskar Van Deventer, and Hans J Frankena. Modeling and characterization of an electrooptic polarization controller on linbo/sub 3. *Journal of lightwave technology*, 11(7):1151–1157, 1993.